Cement and Concrete Research 158 (2022) 106852

Contents lists available at ScienceDirect

Cement and Concrete Research

journal homepage: www.elsevier.com/locate/cemconres

Variation of self-cleaning performance of nano-TiO_2 modified mortar caused by carbonation: From hydrates to carbonates

Zixiao Wang [a,b], Qingliang Yu [a,b,*], Pan Feng [c,d], H.J.H. Brouwers [b]

[a] School of Civil Engineering, Wuhan University, Wuhan 430072, PR China
[b] Department of the Built Environment, Eindhoven University of Technology, 5600 MB Eindhoven, the Netherlands
[c] Jiangsu Key Laboratory of Construction Materials, School of Materials Science and Engineering, Southeast University, Nanjing 211189, PR China
[d] State Key Laboratory of High Performance Civil Engineering Materials, Nanjing 210008, PR China

ARTICLE INFO

Keywords:
Nano TiO_2 hydrosol
Concrete carbonation
Photocatalytic self-cleaning surface
Confocal Raman Microscopy
Prediction model

ABSTRACT

Evaluation and quantification of the effects of the carbonation process on photocatalytic activity are essential for the long-term functional assurance of nano TiO_2 modified photocatalytic concrete. This work focuses on the photocatalytic self-cleaning performance variation of mortar containing different dosages of nano TiO_2 hydrosol at different carbonization duration. The colourimetric analysis is used to evaluate the self-cleaning performances of carbonated mortar samples. The distribution areas of anatase TiO_2, hydrates, and carbonates in the mortar surface are characterized by the Confocal Raman Microscopy. The data recorded during the 28 days of carbonation show that the self-cleaning performance of mortar surfaces features a recovery phenomenon during carbonation. The correlations between photocatalytic self-cleaning performance and the possible parameters are analysed. A predictive model is suggested to evaluate the influence of carbonation degree on the photocatalytic self-cleaning ability of nano TiO_2 hydrosol modified mortar.

1. Introduction

Nano TiO_2-based photocatalytic cement-based materials have proved excellent air purification and self-cleaning performance in previous studies and field applications [1–8], and among the available forms, hydrosol TiO_2, thanks to its fine size of 5 to 100 nm [17–20], has shown better depollution performance than other types [9–13]. However, the photocatalytic ability of nano TiO_2 modified cement-based materials can be weakened by the physio-chemical reactions during the service. Among those reactions, carbonation-induced cement hydrates alteration is potentially a serious issue [14–16], which includes a series of complex physical and chemical-related dissolution-precipitation reaction processes [17–21], affecting the durability of concrete structures [21–26]. The photocatalytic depollution rates of fully carbonated photocatalytic mortar samples have been reported to reduce significantly [14,15,27,28], for example, about 50% [26]. The shielding effect and filling effect of calcium carbonates in carbonated mortar are the main possible reasons for the decrease in photocatalytic performance [27].

The carbonation process of cement-based materials is influenced by CO_2 concentration, temperature [29], relative humidity, the types of supplementary cementitious materials [30] and the diffusion ability of CO_2 in the matrix, among which the CO_2 concentration [18,21,31–33] and relative humidity [31,34–36] significantly affect the chemical changes and crystal phases of cement hydrates during carbonation. In the natural environment with a CO_2 concentration of about 0.03%, it will take several years for the total carbonation of cement hydrates in the depth of 10 mm to take place [37–39], indicating that the phase and crystal shape from hydrates to calcite crystals experience continuous changes during a very long period. During carbonation, the cement hydrates in mortar usually transform into different forms of calcium carbonate ($CaCO_3$) based on the initial conditions, such as the crystal shapes and morphology of the mortar. Calcium carbonate has polymorphic forms [40–43], with different crystal sizes, shapes, and molecular volumes. Calcite, vaterite, and aragonite are the three anhydrous crystalline polymorphs of $CaCO_3$. The calcium carbonate hexahydrate (Ikaite, $CaCO_3 \bullet 6H_2O$) and calcium carbonate monohydrate ($CaCO_3 \bullet H_2O$) are the two well-defined hydrated crystalline polymorphs of $CaCO_3$. The amorphous $CaCO_3$ also contains a variety of forms. Table 1 summarises the parameters such as density and molar volume of cement hydration products and carbonation products.

The carbonation reactions of Portlandite and products crystal

* Corresponding author at: School of Civil Engineering, Wuhan University, Wuhan 430072, PR China.
E-mail address: q.yu@bwk.tue.nl (Q. Yu).

https://doi.org/10.1016/j.cemconres.2022.106852
Received 8 November 2021; Received in revised form 20 April 2022; Accepted 18 May 2022

Table 1
Compounds participating in the carbonation reactions.

Name	Molecular formula	Density (g/cm^3)	Molar weight (g/mol)	Molar volume (cm^3/mol)
Portlandite	$Ca(OH)_2$	2.23	74	33.18
C-S-H	$(CaO)_{1.7}(SiO_2)(H_2O)_{1.80}$	2.60	187.6	72.15
Calcium carbonate hydroxide (CCH1)	$Ca_3(CO_3)_2(OH)_2$	1.60	274	171.25
Defernite (CCH2)	$Ca_6(CO_{2.65})_2(OH_{0.657})\bullet 7(H_2O)_2$	2.50	501.4	200.56
Calcium carbonate hydroxide hydrate (CCH3)	$Ca_3(CO_3)_2(OH)_2\bullet 1.5H_2O$	1.82	301	165.38
Ikaite (CCH4)	$CaCO_3(H_2O)_6$	1.78	208	116.85
Monohydrocalcite (CCH5)	$CaCO_3(H_2O)$	2.38	118	49.58
Vaterite	$CaCO_3$	2.54	100	39.37
Aragonite	$CaCO_3$	2.93	100	34.13
Calcite	$CaCO_3$	2.71	100	36.90
Silica gel	SiO_2	2.2	60	27.27

systems suggested by Stepkowska [44] are shown in the following equation:

$$\underset{\text{hexagonal}}{\text{Portlandite}} \rightarrow \underset{\text{orthorhombic monoclinic}}{\text{CCH1}\rightarrow\text{CCH2}\rightarrow\text{CCH3}} \rightarrow \underset{\text{monoclinic}}{\text{CCH4}} \rightarrow \underset{\text{hexagonal}}{\text{CCH5}} \rightarrow \underset{\text{hexagonal}}{\text{vaterite}} \rightarrow \underset{\text{orthorhombic}}{\text{aragonite}} \rightarrow \underset{\text{rhombohedral}}{\text{calcite}} \quad (1)$$

The interplanar crystal spacing d[*hkl*] of $Ca(OH)_2$ firstly increases when CCH1, CCH2, and CCH3 are formed. The crystal shape and size of $Ca(OH)_2$ significantly influence the polymorph evolution during the conversion of $Ca(OH)_2$ into $CaCO_3$. As to the C-S-H phase, the crystal pattern and shape of carbonation products are influenced by the Ca/Si ratio [25], mineral morphology [17], and density [19]. The molar volumes of these intermediate carbonization products CCH1 to CCH4 are several times larger than the volumes of the CH and C-S-H. The volume of reactants and products involved in carbonation first increases sharply and then decreases gradually from hydration products to the final stable state of calcite.

The volume variation of calcium carbonates caused by carbonation of cement hydrates will vitally influence the microstructure of photocatalytic mortar, consequently leading to alteration of its self-cleaning performance. However, only a few researchers [14,15,27,28] studied the influences of fully carbonated cement hydrates on the photoactivity of powder-formed nano TiO_2 in cement-based materials. Therefore, studying the phases and morphology of cement hydrates in photocatalytic self-cleaning mortar during carbonation is essential to understand the functional ability during the engineering application.

This work investigates the potential relationships between crystalline morphology evolutions and the photoactivity reductions to control the adverse effects of carbonation on photocatalytic cement-based materials. The accelerated carbonation test with 3% CO_2 and 65% RH is used to mimic the natural environment as the variation of the microstructure of ordinary Portland cement paste upon accelerated carbonation is relatively close to that of paste in the natural carbonation [18,21]. The chromatics and optical photocatalytic factors are determined to characterize the self-cleaning performance of mortar samples. More importantly, a calculation model is established to quantitatively evaluate the influence on the photocatalytic self-cleaning performance declination caused by carbonation of hydrates.

2. Materials and experimental

2.1. Materials

The nano dispersed anatase TiO_2 hydrosol is synthesized based on the method in our previous study [45]. The hydrodynamic size of TiO_2 hydrosol is 18.92 ± 6.358 nm, and the percentage of pure TiO_2 in hydrosol is 1.54 wt%. CEM I 52.5 R cement, standard sand (CEN-EN 196–1), and tap water are used to prepare the mortar samples with the water to cement ratio mass of 0.5 and sand to cement mass ratio of 3. The chemical composition of cement is shown in Table 2, which is tested by X-ray fluorescence spectroscopy.

The samples are wet mixed for five minutes before moulded in 4 cm × 4 cm × 16 cm moulds and covered with a plastic sheet. Different amounts of TiO_2 hydrosol are firstly dispersed in the mixing water. The TiO_2 to cement mass ratios are 0%, 0.01 wt%, 0.05 wt%, 0.10 wt% and 0.50 wt%, respectively. After one day of curing, the samples are demoulded and cured in a climate chamber (RH > 95%, 20 °C) until 28 days.

2.2. Methods

2.2.1. Accelerated carbonation tests

For the accelerated condition, mortar samples are placed in a CO_2 incubator (HPP, Memmert, Germany) in which the CO_2 concentration is maintained at 3 ± 0.1%, the relative humidity at 65 ± 0.1% and the temperature at 25 ± 0.1 °C. Four different carbonation test durations are set as 3 days, 7 days, 14 days, and 28 days for testing the mortar samples. Before the accelerated carbonation tests, both ends of the prism sample are cut with 1 cm and then cut into three cubes with a side length of 4 cm. For achieving one-dimensional carbonization, the four side faces of each cube are sealed by paraffin and Parafilm (Bemis Company Inc., United States). Before that, the cubes are dried at 40 °C in the oven for 48 h. Two parallel samples are used in each test group.

2.2.2. Self-cleaning tests

The self-cleaning performances of the TiO_2 modified mortar slice samples are evaluated by the colourimetric analysis of the degradation of the organic dye Rhodamine B (RB). Each surface area of the paste sample is stained by painting 600 μL of 50 mg/L RB aqueous solution. Then the samples are kept overnight in the dark at room temperature for drying. Subsequently, the samples are exposed to a UV lamp (10 ± 0.05 W/m^2) to simulate UV light in natural conditions, and the discolouration of the samples is monitored. The UV lamb is composed of three UV tubes with the power of 25 W, the UV-A wavelength ranges from 300 nm to 400 nm, centered at 345 nm. The reflected colour measurements are taken on the sample's surface with a spectrometer (USB4000, Ocean optics, United Kingdom) equipped by a light resource with a wavelength range from 380 to 780 nm. For mortar with each dosage of nano TiO_2, two slices are used as the parallel samples. Nine points are recorded for the colorimetric tests for each sample, and each point is tested four times. The colour of each sample is measured after 0.5 h, 1 h, 2 h, 4 h, 8 h, 16 h and 26 h of UV irradiation, respectively. The percentage of discolouration of RB on the surface of mortar (R_t) is expressed with a* value coordinate of the dominant colour of dye in the CIE Lab colour space, according to.

$$R_t = [(a_0^* - a_t^*)/a_0^*] \times 100 \quad (2)$$

Table 2
Chemical composition of CEM I 52.5 R cement.

Compound	CaO	SiO_2	Fe_2O_3	SO_3	Al_2O_3	MgO	K_2O	TiO_2	P_2O_5	Minor elements[a]
Content (%)	66.34	18.22	3.81	3.15	5.56	1.68	0.29	0.50	0.16	0.30

[a] $V_2O_5 + Cr_2O_5 + MnO + CuO + ZnO + BaO + Cl$.

Where, a_0* is the value of a* at time 0 before irradiation, a_t* is the value after t hours irradiation. According to [46], a material or surface is regarded as photoactive only if $R_4 > 20\%$ and $R_{26} > 50\%$.

2.2.3. Characterizations

An isothermal calorimeter (TAM Air, TA Instruments, United States) is used to record the heat release of cement hydration containing different concentrations of TiO_2 hydrosol every 10 s for the first 168 h of hydration. The test temperature is 20 °C.

The planetary ball mill (Pulverisette 4, Fritsch, Germany) is used to prepare the powder samples from the slice mortar specimens. Then the powder samples are sieved through a fine sieve with the pore size of 75 μm. The fine powders are dried at 40 °C for 48 h before the X-ray diffraction and TG analysis. For mortar samples carbonized for different periods, one slice mortar sample is crushed for preparing powder sample.

The crystal patterns of cement hydrates before and after the accelerated carbonation test are determined by the X-ray diffraction (XRD) pattern (Bruker D4 PHASER, Philips, The Netherlands) with a Co tube (40 kV, 40 mA), with the test step size of 0.02°/min and dwell time of 0.5 s. According to the previous study [47], the crystals of the Portlandite with hexagonal-prism shape faceted by {10-10} prismatic and {0001} basal facets, and the exhibit aspect ratio (r_L) of the crystal can be calculated by:

$$r_L = \frac{L_1}{L_2} \tag{3}$$

Where L_1 is the characteristic linear size of portlandite crystal in {10-10} growth direction; L_2 is the characteristic linear size of portlandite crystal in {0001} growth direction.

A nitrogen adsorption-desorption device (TriStar II 3020, Micrometeritics, USA) is used to test the nitrogen sorption isotherm and Brunauer, Emmett and Teller (BET) specific surface area of the mortar samples. The Barrett-Joyner-Halenda (BJH) plots are analysed to evaluate the pore size distribution. Before the BET test, the slice mortar samples are cut into small blocks with a volume of about 0.5 cm^3 and then dried at 40 °C for 48 h in the oven, finally degassed in an external degassing station at 40 °C under N_2 flow for 4 h. The mass of each tested sample is about 0.60 g, and the test pressure ranges from 0.01 to 0.14 atm.

A Quanta 250 FEG scanning electron microscope (ThermoFisher Scientific, USA) and a Phenom Pro Desktop scanning electron microscope (ThermoFisher Scientific, USA) are used to capture the morphology images of mortar samples with secondary electrons detector. The slice mortar samples are cut into blocks of about 1 cm^3 and dried at 40 °C for 48 h before being put into the SEM test chamber.

The UV–vis diffuse reflectance spectra (UV–vis DRS) of TiO_2 hydrosol modified mortar before and after accelerated carbonation tests are measured by a UV-VIS-NIR spectrophotometer (Lambda 750, Perkin Elmer, USA), the tested range is 200 nm to 2500 nm, 2 nm per second. Two mortar slices are used as the parallel samples for obtaining the reflectance spectra. All the samples are dried at 40 °C for 48 h before tests. The Kubelka-Munk optical absorption coefficient F(R) and the bandgap energy (E_g) of TiO_2 modified cement paste samples are calculated by Tauc's relation [48]. The exponential character of the absorption coefficient near the absorption edge is expressed by the Urbach rule [49,50]. Detailed information can be found in our previous work [45].

The distribution of phases on TiO_2 hydrosol modified mortar is observed by Confocal Raman Microscopy (Witec alpha300S, Witec, Ulm, Germany). The Raman spectra range from 0 cm^{-1} to 3900 cm^{-1}. The 532 nm excitation laser with a power of 60 mW is used in measurements. The scan area on the surface of mortar is 35 μm × 35 μm, the size of the Raman images is 70 × 70 pixels with an integration time per pixel of 0.1 s. One mortar slice is used for CRM mapping analysis.

The TG analysis of mortar samples before and after the accelerated carbonation is conducted using a STA 449 F1 instrument (NETZSCH, Germany) with N_2 as the carrier gas by heating up to 1000 °C from 40 °C at the rate of 10 °C/min. The TGA plots of cement hydrates are usually divided into three main parts [51–53]: (1) The primary range of dehydration of C-S-H gel is 105 °C to 300 °C. (2) Dehydroxylation of calcium hydroxide (CH) is 400 °C to 500 °C. (3) Decarbonisation of calcium carbonate ($CaCO_3$). The decomposition of $CaCO_3$ in the range of 500 °C to 680 °C is related to the amorphous calcium carbonate [54,55]. The poorly-crystalline (including vaterite and aragonite phases) and well-crystalline $CaCO_3$ (calcite phase) are considered to be decomposed between 680 °C and 780 °C, and between 780 °C and 990 °C, respectively [56]. The carbonation degree (D_c) of mortar can be calculated as follows [57]:

$$D_c = \frac{C - C_0}{C_{max} - C_0} \times 100\% \tag{4}$$

C is the amount of CO_2 in the sample (refer to the CO_2 derived from the $CaCO_3$); C_0 is the amount of CO_2 in the non-carbonated sample; C_{max} is the theoretical amount of carbon dioxide needed to combine with the total CaO in the sample to form $CaCO_3$. The C_{max} must be analysed by a reliable method, such as XRF, and the CaO amount in the $CaCO_3$ of raw materials should be deducted.

3. Results

3.1. Cement hydrates and carbonates

3.1.1. Hydration kinetics

The influence of TiO_2 hydrosol concentration on the Portland cement hydration kinetics at the early age is studied, and the cumulative heat release and hydration rate are shown in Fig. 1. At a low concentration of TiO_2, for example, 0.01 wt% of cement, the cumulative hydration heat is primarily unaffected. While with the increase of the concentration of TiO_2 hydrosol, the total released hydration heat decreases clearly, as seen in Fig. 1(A). Moreover, the TiO_2 hydrosol reduces the hydration rate, delays the appearance of the second heat flow peak and extends the acceleration and deceleration periods of cement hydration. The peak value and cumulative heat release of cement are significantly reduced by adding TiO_2 hydrosol at higher concentrations, while the width of the hydration heat flow peak increases with the dosages of nano TiO_2. In the paste containing 0.50 wt% TiO_2, the heat flow peak appears about 12 h later than in the reference paste. It is concluded that the presence of TiO_2 hydrosol retards the hydration of Portland cement, prolongs the induction period of early hydration of cement, and reduces the hydration rate in the acceleration and deceleration periods. When TiO_2 hydrosol to cement ratio is less than 0.1 wt%, the influence of TiO_2 hydrosol on the hydration heat evolution becomes very small after three days.

However, it should be noticed that the retardation of cement hydration may influence the hydrates crystal pattern and morphology after 28 days of curing, which will be discussed in the following section.

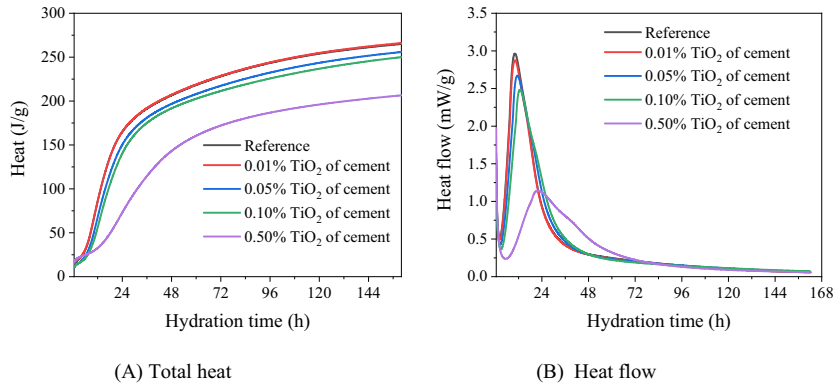

Fig. 1. Influence of TiO_2 hydrosol on the exothermic heat flow and total heat of per gram of cement
(A) Total heat
(B) Heat flow.

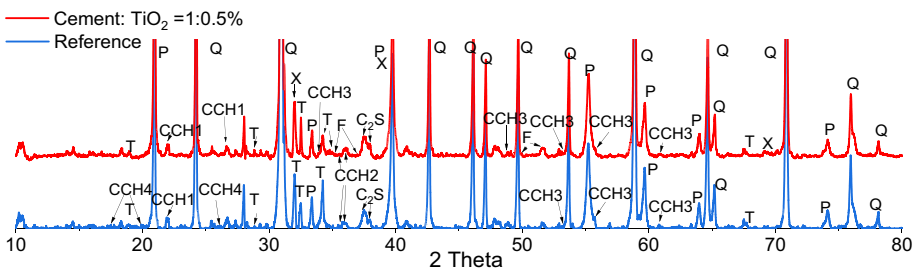

Fig. 2. X-ray diffractograms of mortar with and without TiO_2 hydrosol before carbonation.
Symbols: Portlandite: P, Quartz: Q, Tobermorite: T, Hillebrandite: H, Xonotlite: X, Foshagite: F, Calcium carbonate hydroxide: CCH1; Defernite: CCH2; Calcium carbonate hydroxide hydrate: CCH3; Ikaite: CCH4; Monohydrocalcite: CCH5.

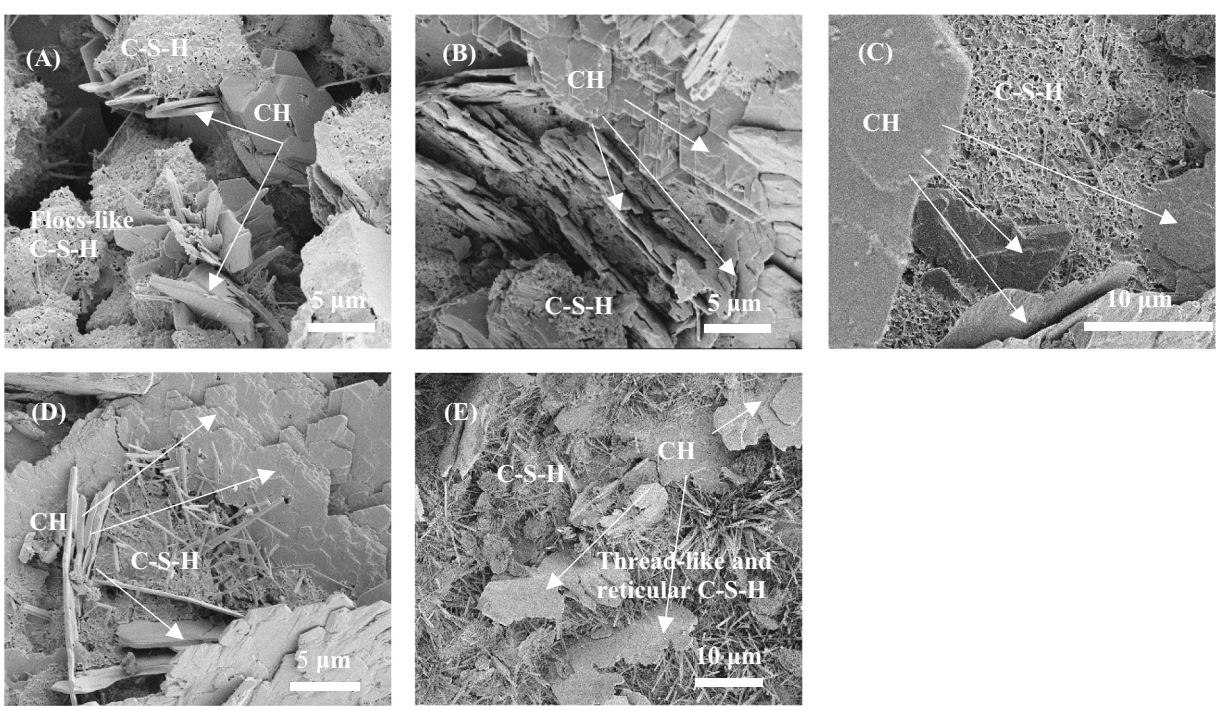

Fig. 3. Morphology of Portlandite crystal in the mortar after curing with different amount of TiO_2 hydrosol; (A) 0 wt% TiO_2; (B) 0.01 wt% TiO_2; (C) 0.05 wt% TiO_2; (D) 0.10 wt% TiO_2; (E) 0.50 wt% TiO_2.

3.1.2. Hydration products

The X-ray diffractograms of reference mortar and mortar samples containing 0.5 wt% TiO_2 before are shown in Fig. 2. Before carbonation, the main hydrates of calcium hydroxide (CH) and C-S-H phases are detected in the TiO_2-modified mortar and the reference mortar. The C-S-H phases in mortar sample containing 0.50 wt% TiO_2 contains Tobermorite, Hillebrandite, Xonotlite, and Foshagite phases, while only the Tobermorite phase is detected in the reference mortar sample. Based on the previous study [45] and the results in Section 3.1.1, the reason that the formation of C-S-H phases are delayed and the morphologies of C-S-H phases are different at an early age is because the nano TiO_2 hydrosol has the surface functional groups of $–COO^-$ and –C–OH.

As shown in Fig. 3, the morphology of the C-S-H gel is also influenced by the applied TiO_2. In the mortar with a lower content of TiO_2 (<0.10 wt%), a foil-like C-S-H gel is observed. In the mortar with 0.10 wt% TiO_2, the fibrillar and reticular C-S-H phases appear, which co-exist with foil-like C-S-H and CH crystals. More fibrillar C-S-H gels appear when the mortar contains 0.50 wt% TiO_2. Previous studies [58,59] have reported a similar phenomenon: nano TiO_2 in the forms of sol and suspension leads to fibrillar C-S-H that contains alumina with a high Ca/Si ratio (~2) in the hardened cement paste. Furthermore, the initial Ca/ Si ratios of C-S-H gel in hydrates are closely related to its carbonation rate, the C-S-H with higher Ca/Si ratios shows a faster carbonation rate than the lower Ca/Si ratios [60]. Therefore, the results in Fig. 2 and Fig. 3 support that the ratios of Ca/ Si in the C-S-H phase are influenced by the amount of nano TiO_2 hydrosol, which will affect the carbonation rate and the morphology of carbonates in mature cement-based materials [25,61].

Fig. 4(A) shows the XRD pattern of mortar samples containing different content of nano TiO_2, the typical peaks of Portlandite at {0001}, {10–10} and {10−11} planes appear on the patterns of the reference mortar and TiO_2 modified mortar before carbonation test. In other words, the presence of TiO_2 hydrosol does not affect the lattice parameters of portlandite crystals and does not change the types of cement hydrates. Nevertheless, in the mortar containing a lower content of TiO_2, the intensity of facets of {0001} increases slightly. While at higher contents of TiO_2, the intensity of facets of {0001} exhibits a much sharper peak. In Fig. 4(B), the exhibit aspect ratios (r_L) of CH crystal, that is the intensity ratio of {0001}/ {10–10}, increase with the increased content of TiO_2 in the mortar, which corresponds well with the shape change in portlandite crystal [47]. Typically the portlandite crystals are detected in the shape of hexagonal tabular [47,62–64] (Fig. 4(B), pattern a). A larger ratio of r_L indicates a shorter length of crystal along the *c* axis and a more prominent basal facet (shown in Fig. 4 (B), pattern c). The SEM images of Portlandite crystal in the mortar are shown in Fig. 3. As seen in Fig. 3(A), the CH crystal is the typical hexagonal tabular with a small area of {0001} basal facet, and the edge of a single CH crystal is relatively regular. With the increase of TiO_2 amount in the mortar, the CH crystals tend to grow in layers, the boundary edges of layers tend to be indistinct, and the amount and area of {0001} basal facet increase. These SEM images of CH crystals confirm that the CH crystals grow into layered thin hexagonal plates in the presence of a higher amount of TiO_2 hydrosol in the mortar, as illustrated in Fig. 4(B).

According to previous studies about the formation mechanisms of stable calcite from Portlandite [63,65,66], calcite can directly nucleate and grow after the dissolution of amorphous $CaCO_3$, vaterite and aragonite, or it can nucleate on vaterite and aragonite, then grow via non-classical particle-mediated aggregation or a classical ion-mediated mechanism. Thus, the precipitation of $CaCO_3$ is dominated by the crystal shape and size of Portlandite, atomic defects [67], and environmental conditions like relative humidity [68], temperature [41], water content and the parameters of pore solution, such as the degree of supersaturation and ion activity [69]. Based on the modified Kelvin equation [70,71], larger CH crystals have lower solubility than smaller crystals, resulting in a slower dissolution of CH in CO_3^{2-} saturated pore solution when CO_2 dissolves into the pore solution of mortar. Furthermore, according to [65], the polymorph evolution of calcium carbonate is slower for larger CH crystals. Thus, the presence of TiO_2 hydrosol in the mortar sample will retard the carbonation of CH because of the larger crystalline size and smaller specific surface area.

3.1.3. Carbonation products

Fig. 5 shows the X-ray diffractograms of all mortar samples containing different concentrations of TiO_2 hydrosol before and after carbonation at 28 days. It is seen that, after 28 days of carbonation, the prominent intensity peak of Portlandite in all mortar samples decreases significantly. The CCH1, CCH2, CCH3 and CCH5 peaks are observed in both mortar samples, proving that the intermediate reactions between Portlandite and CO_2 are still ongoing. These results confirm the slower carbonation reaction rate of CH crystals with layered thin hexagonal plates with significant {0001} basal facet and lower specific surface area.

The calcite and two kinds of meta-stable aragonite and vaterite phases are detected in the mortar sample containing 0.50 wt% TiO_2 hydrosol. In contrast, no aragonite peak is detected in the reference mortar samples. According to Black et al. [25], the CaO to SiO_2 ratio (Ca/Si) significantly influences the carbonation products of the synthetic C-S-H(I). When the Ca/Si > 1, the amorphous $CaCO_3$ is always the initial carbonation product, and then the aragonite phase is precipitated with the formation of SiO_2 gel. The initial carbonation product of the C-S-H with Ca/Si of 0.75 and 0.67 is amorphous $CaCO_3$, together with the traces of vaterite. Therefore, it can be deduced that the Ca/Si ratio of C-S-H in the blank mortar is higher than one in the mortar containing 0.5 wt% of nano TiO_2 hydrosol. The phases of carbonation products also confirm that the C-S-H with a high Ca/Si ratio largely exists in the mortar sample with 0.5 wt% of nano TiO_2 hydrosol. Because the C-S-H

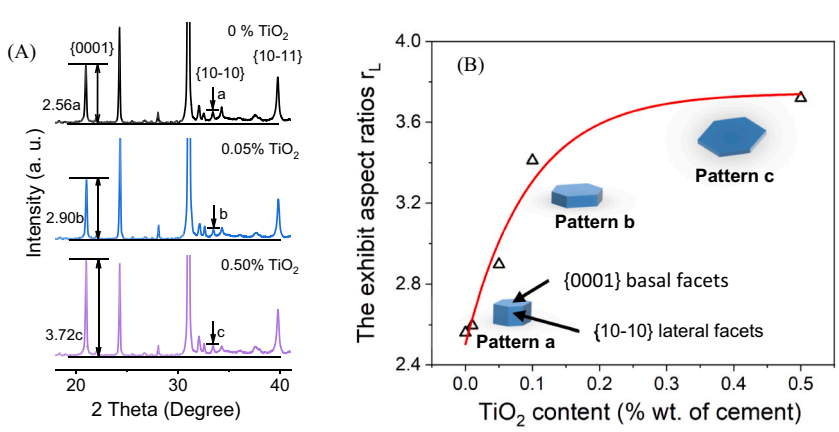

Fig. 4. (A) Crystal pattern of hydrates before carbonation test; (B) Plot of the exhibit aspect ratios (r_L) of CH vs. TiO_2 mass fraction.

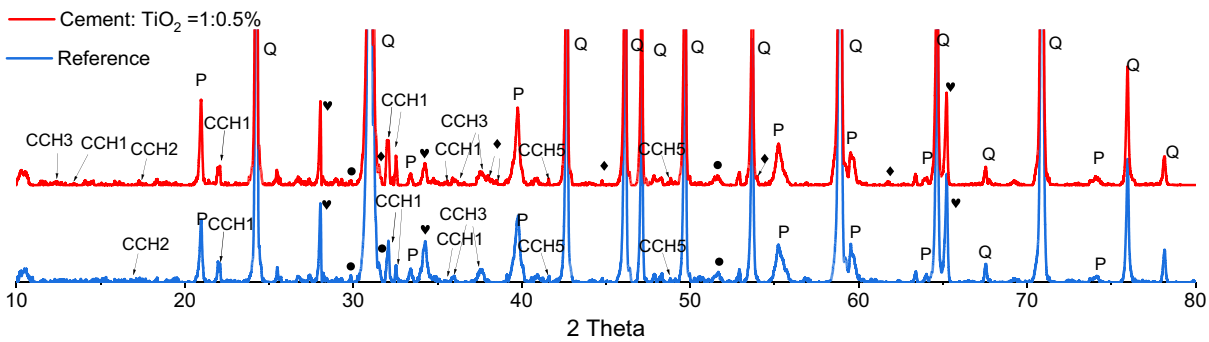

Fig. 5. X-ray diffractograms of mortar with and without TiO_2 hydrosol after 28 days of carbonation test.
Symbols: Portlandite: P; Quartz: Q; Calcite: ♥; Aragonite:◆; Vaterite: •; Calcium carbonate hydroxide: CCH1; Defernite: CCH2; Calcium carbonate hydroxide hydrate: CCH3; Ikaite: CCH4; Monohydrocalcite: CCH5.

with a higher Ca/Si shows a faster dissolution rate [72], the carbonation rates for C-S-H should increase with the increase of Ca/Si [60].

Based on the above analysis, the presence of TiO_2 hydrosol leads to more CH with larger crystal size and more fibrillar-like C-S-H, which have opposite effects on the carbonation rate of the mortar samples. Thus, it could be hypothesized that when the retardation effect of CH phase prevails, the carbonation rate would be slower; when the acceleration effect of the C-S-H phase prevails, the carbonation rate would be faster. The carbonation degree of mortar will be discussed in Section 3.4. The specific surface area of mortar is another significant factor for CO_2 attack. The presence of nano TiO_2 with different concentrations in mortar also affects the variation of the specific surface area of the mortar sample, which will be discussed in Section 3.2.

3.2. BET specific surface area of mortar

As discussed in Section 3.1, the crystal size and morphology of main cement hydrates after curing are significantly influenced by nano TiO_2 hydrosol, reflected by the variation of specific surface area (SSA) of hardened mortar. Fig. 6 presents the BET SSA of mortar with and without TiO_2 hydrosol before and after different carbonation duration. Before carbonation, the SSA of mortar samples increases with the mass content of TiO_2 hydrosol, indicating TiO_2 hydrosol promotes dissolution and subsequent carbonation. The initial crystal morphology of CH and C-S-H phases in TiO_2 modified mortar influences the SSA during the carbonation. After 28 days of curing, the SSA of the mortar increases with the increase of TiO_2 content, confirming again that the morphology

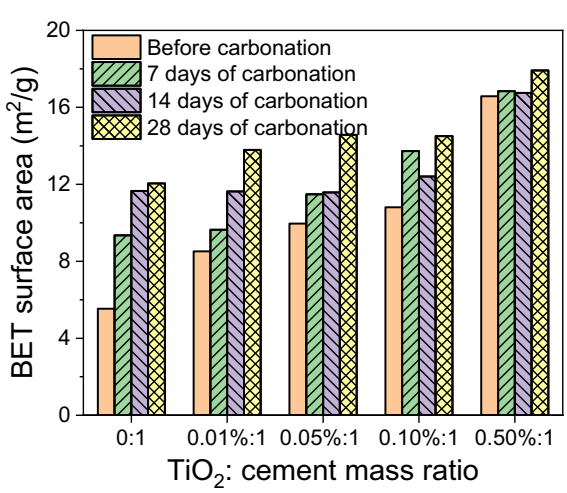

Fig. 6. BET surface area of mortar samples containing different amount of nano TiO_2 undergo different duration of accelerating carbonation test.

of cement hydrates is affected by the added TiO_2 hydrosol.

The SSA of mortar in each group increases with the increase of carbonation time, attributed to the molar volume difference between the cement hydrates and the formed $CaCO_3$ [21]. In Fig. 6, the SSA of the mortar samples with 0.50 wt% of TiO_2 hydrosol is less influenced by carbonation. While in the mortar with a lower content of TiO_2 (<0.1 wt %), the SSA increases obviously with the increase of carbonation duration, attributing to the less molecular volume variation of carbonates in the mortar with 0.50 wt% of TiO_2 hydrosol during carbonation. The $CaCO_3$ with different crystalline states shows quite different crystal morphology, which also influences the SSA of mortar. As discussed in Section 3.1.3, it could be inferred that the carbonation rate of C-S-H plays the leading role, and there are more crystalline phases of calcium carbonate in the mortar with 0.50 wt% of TiO_2 hydrosol during carbonation. These results confirm that the presence of TiO_2 hydrosol influences the volume difference between the hydrates and the carbonation products.

3.3. Carbonation degree of mortar

The mass loss of mortar samples containing 0.01 wt% and 0.50 wt% of TiO_2 upon different carbonation duration are shown in Fig. 7. The plots of the reference mortar sample and mortar sample containing 0.05 wt% and 0.10 wt% of TiO_2 are shown in Fig. S5 in the supplemental file. The mass loss curves shown in Fig. 7 and Fig. S5 are obtained by TGA. As shown in Fig. 7, the temperature ranges of the endothermic peaks of C-S-H gel, CH in all test mortar powder samples are relatively stable, while the endothermic peaks of poorly crystalline $CaCO_3$ in the test mortar containing lower TiO_2 (<0.1 wt% of cement) moves towards the lower temperature. These results reveal that the concentration of nano TiO_2 hydrosol influences the thermo-stability of newly formed poorly crystalline $CaCO_3$. The mass ratios of amorphous $CaCO_3$ (ACC), poorly crystalline $CaCO_3$ (vaterite and aragonite), and well-crystalline $CaCO_3$ (calcite) in TiO_2 modified mortar at different carbonation time are shown in Fig. 8. The ACC and poorly crystalline $CaCO_3$ increase with the carbonation time, while the increase rate of calcite is slower in the reference mortar without TiO_2 hydrosol. With the increased content of TiO_2 hydrosol in the mortar, the increase rate of ACC is lower than that of crystalline $CaCO_3$, indicating that the existence of TiO_2 hydrosol can accelerate the transformation from ACC to calcite. As shown in Table 1, the molecular volume of calcite is smaller than the mean molecular volume of poor-crystalline calcium carbonates (vaterite and aragonite). Fig. 10 proves that before carbonation the mortar containing 0.50 wt% of TiO_2 has more well-crystalline $CaCO_3$ and less poorly crystalline $CaCO_3$, which explains the BET specific surface area results shown in Section 3.2.

The calculated average carbonation degree values (D_c) of mortar containing different amounts of TiO_2 hydrosol are shown in Fig. 9.

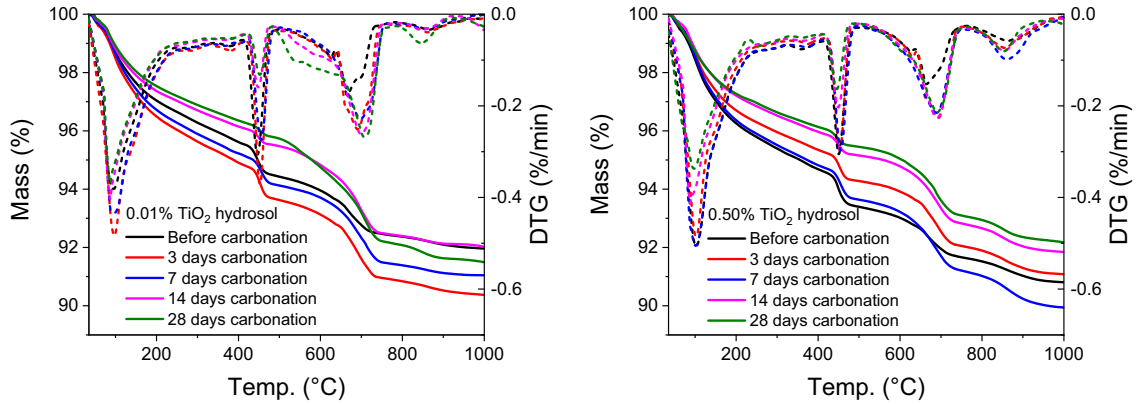

Fig. 7. Mass loss of 0.01 wt% and 0.50 wt% TiO_2 hydrosol modified mortar during carbonation.

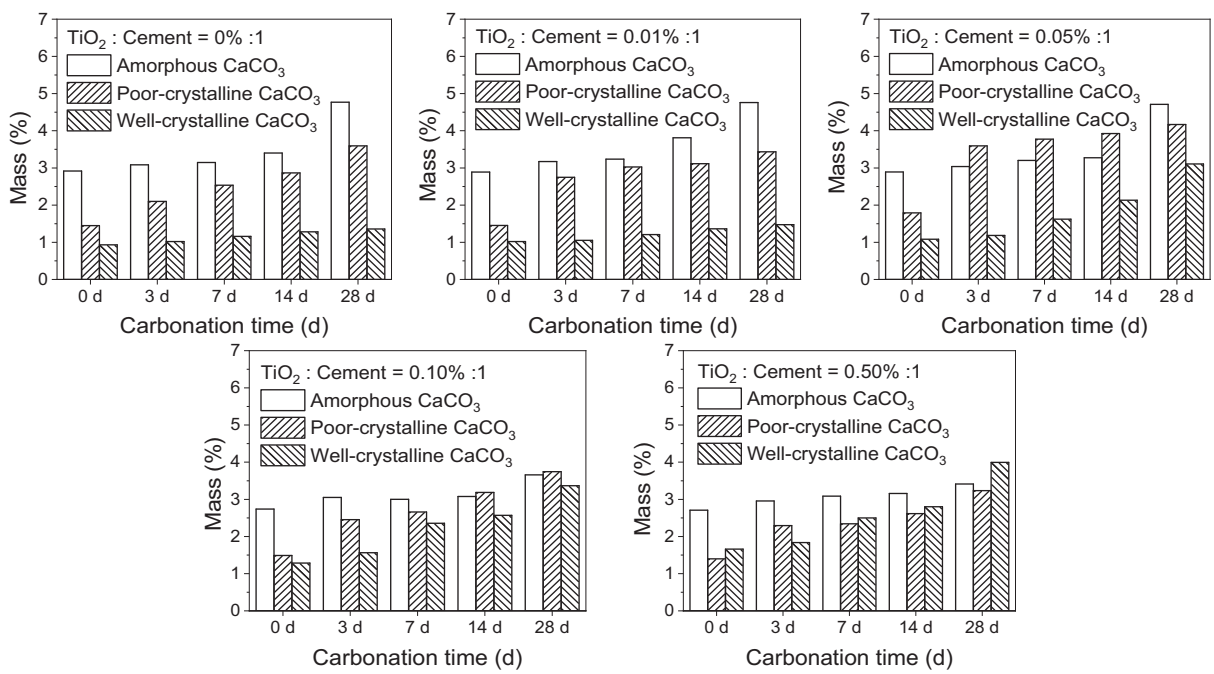

Fig. 8. The mass ratios of amorphous, poorly and well crystalline $CaCO_3$ in test mortar samples during carbonation.

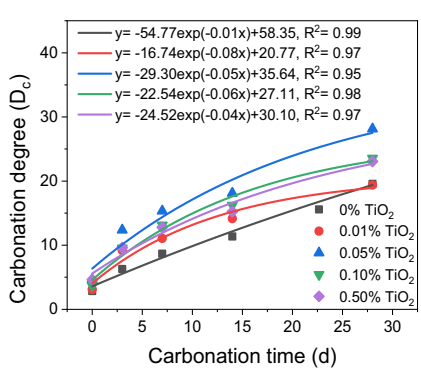

Fig. 9. The carbonation degree of mortar containing different content of TiO_2 after different carbonation time.

Before the carbonation test, the initial D_c of mortar samples containing TiO_2 hydrosol is close to the reference mortar. During the carbonation, the D_c of the mortar increases with the content of TiO_2 when the dosage is lower than 0.05% wt% of cement, while the D_c values of mortar are close when the TiO_2 dosage is higher than 0.05% wt% of cement. These results prove the hypothesis in Section 3.1.2 that the carbonation rates of CH and C-S-H in the mortar samples show an opposite trend with the increase of nano TiO_2 in mortar. Thus, when the TiO_2 hydrosol concentration is lower than 0.05 wt%, the carbonation rate of CH dominates the mortar carbonation, while when the TiO_2 hydrosol concentration is higher than 0.05 wt%, the carbonation rate of C-S-H dominates the mortar carbonation. In sum, the presence of TiO_2 hydrosol influences the carbonation of C-S-H and CH phases, resulting in different $CaCO_3$ polymorphs in mortar during carbonation. The effects of TiO_2 hydrosol on the microstructure of mortar will be discussed in Section 3.5.

3.4. Self-cleaning performance

3.4.1. Optical photocatalytic factors

The bandgap energy and Urbach energy are used to evaluate the

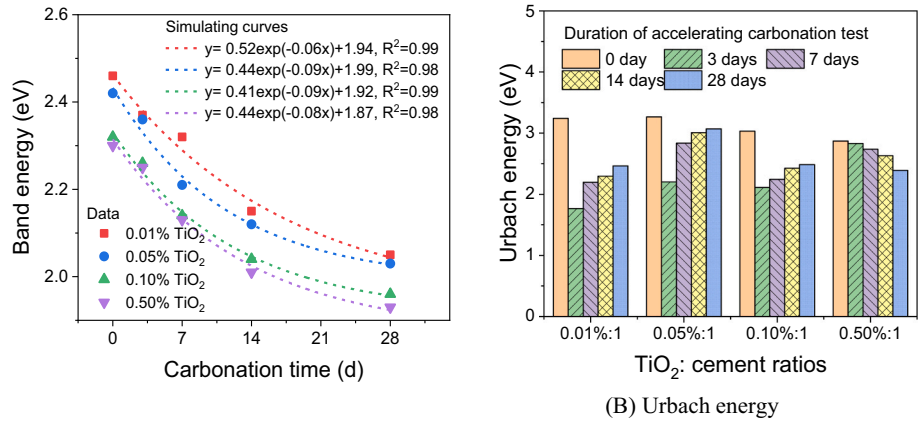

(B) Urbach energy

Fig. 10. The trends of optical bandgap energy and Urbach energy of TiO_2-mortar compounds along with the accelerating carbonation time
(A) Bandgap energy
(B) Urbach energy.

photoactivity of nano TiO_2 [16,73,74]. The change of bandgap energy can represent the electronic structure change of photocatalysts. The Urbach energy can represent the defects and impurities caused by disorders of the electronic structure of photocatalysts when they are doped by metal, non-metal elements [75–77], or cement hydration products [16,78,79]. According to the previous study [14], the photocatalytic performance of nano TiO_2 modified cementitious material is strongly influenced by cement hydration and the age of cement-based materials. The changes in the surface condition of nano TiO_2 particles in hardened mortar influence the photo-induced self-cleaning performance.

Fig. 10 shows the changes of bandgap energy and Urbach energy of TiO_2-mortar compounds at different carbonation duration. The detailed reflectance curves, Tauc's plots and simulating curves for calculating Ubrach energy of mortar samples are shown in Figs. S2 to S4 in the supplemental document. As shown in Fig. 10(A), the bandgap energy of all TiO_2-mortar compounds decreases with the carbonation time exponentially. In TiO_2-mortar samples, the reduction in band edges may be due to locally defective states in the bandgap near the bottom or the top of the TiO_2-mortar conduction band or valence band. These results reflect that the mortar matrix (mainly hydrates and sands) may disrupt the semiconductor electronic structure of the TiO_2 by producing defects [16]. The carbonation of the mortar matrix significantly impacts the structural disorder of mixed nano TiO_2. As shown in Fig. 10(B), when the TiO_2 to cement ratio is lower than 0.10 wt%, the Urbach energy decreases sharply after three days of carbonation and slowly increases during further carbonation. The decrease of bandgap energy indicates that the Urbach tail of TiO_2-mortar compounds increases with the carbonation time. The high value of Urbach energy means that impurities and defects (mainly the Ti^{3+} and oxygen vacancies) make the structure of TiO_2 highly disordered, forming an absorption tail that extends to the depth of the forbidden zone [16,45,80]. In general, the higher the Urbach energy, the better photocatalytic performance of the sample is expected. The following Section 3.4.2 will discuss the self-cleaning performances of TiO_2-mortar samples.

The changes in surface defect status and disorder of the TiO_2-mortar during carbonation also prove that the photocatalytic self-cleaning property of mortar is closely related to the crystal pattern and morphology evolution of main cement hydrates. Section 4 will describe the relationship between the chemical conversions of cement hydrates and the photocatalytic activity of TiO_2-mortar compounds.

3.4.2. Chromatics factors

As to the influences of carbonation on the photo-activity of TiO_2 modified mortar, Fig. 11 shows the change of R_4 and R_{26} on the surface of the mortar at different carbonation duration. Before the accelerated carbonation test, except the sample containing 0.01 wt% of TiO_2, the colour change rates of samples are greater than 25% (R_4) and 50% (R_{26}) after 4 h and 26 h of UV irradiation. These indicate that the low dosage TiO_2 hydrosol modified mortar samples are sufficiently photoreactive before carbonation. Fig. 11(A) shows that although the value of R_4 in each mortar sample decreases with the increase of carbonation time, the R_4 of most mortar samples is still higher than 20%, except for the mortar with 0.01 wt% of TiO_2 after 28 days of carbonation. The influence of hydrates carbonation on the R_{26} value of the mortar sample is more remarkable, as shown in Fig. 11(B). After the first three days of carbonation, the R_{26} value of the mortar with 0.01 wt%TiO_2 is reduced

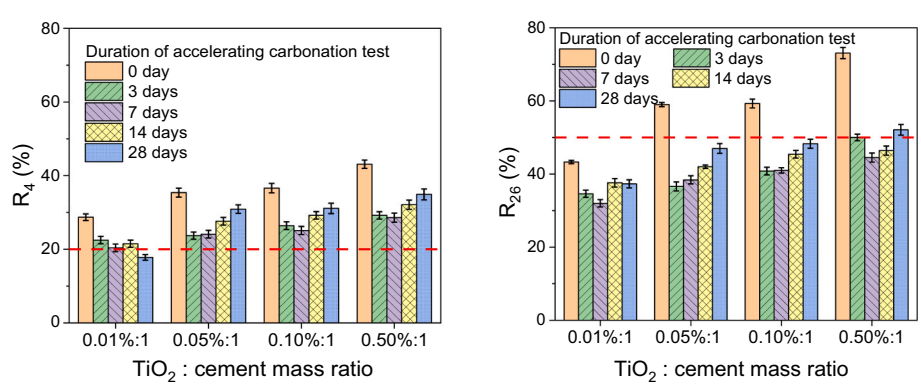

(A) R_4 (B) R_{26}

Fig. 11. Colour change rates R_4 and R_{26} of mortar in each test group.

by 20.1%, while the R_{26} values of the mortar with 0.01 wt% to 0.50 wt% of TiO_2 are reduced by about 30%. However, it is worth mentioning that the R_{26} of mortar with 0.50 wt% decreases after seven days of carbonation and then increases to 52.1% after 28 days of carbonation, while the R_{26} values of mortar with 0.05 wt% and 0.10 wt% TiO_2 starts to increase after three days of carbonation.

It is noted that the TiO_2-mortar sample containing 0.01 wt% of TiO_2 presents similar values of Urbach energy with the sample containing 0.05 wt% of TiO_2, but the RB degradation rate (R_{26}) is not as high as that in the sample containing 0.05 wt% of TiO_2. These may be related to the amount of effective reaction sites and the amount of the RB molecules during the self-cleaning test. When the TiO_2 to cement ratio is between 0.01% to 0.10%, the variation rule of the Urbach energy of TiO_2-mortar is similar to that of R_{26}, as shown in Fig. 11(B). Therefore, the continuous decline of Urbach energy during carbonation will lead to the continuous decrease of photocatalytic self-cleaning performance of photocatalyst, assuming no other factors are involved. However, when the TiO_2 to cement ratio is higher than 0.10%, the R_{26} of mortar slowly upswings after 28 days of carbonation.

In our previous study [45], the surface electron capture effect of hydration products plays an essential role in improving the self-cleaning performance of non-carbonated hardened cement paste with a higher

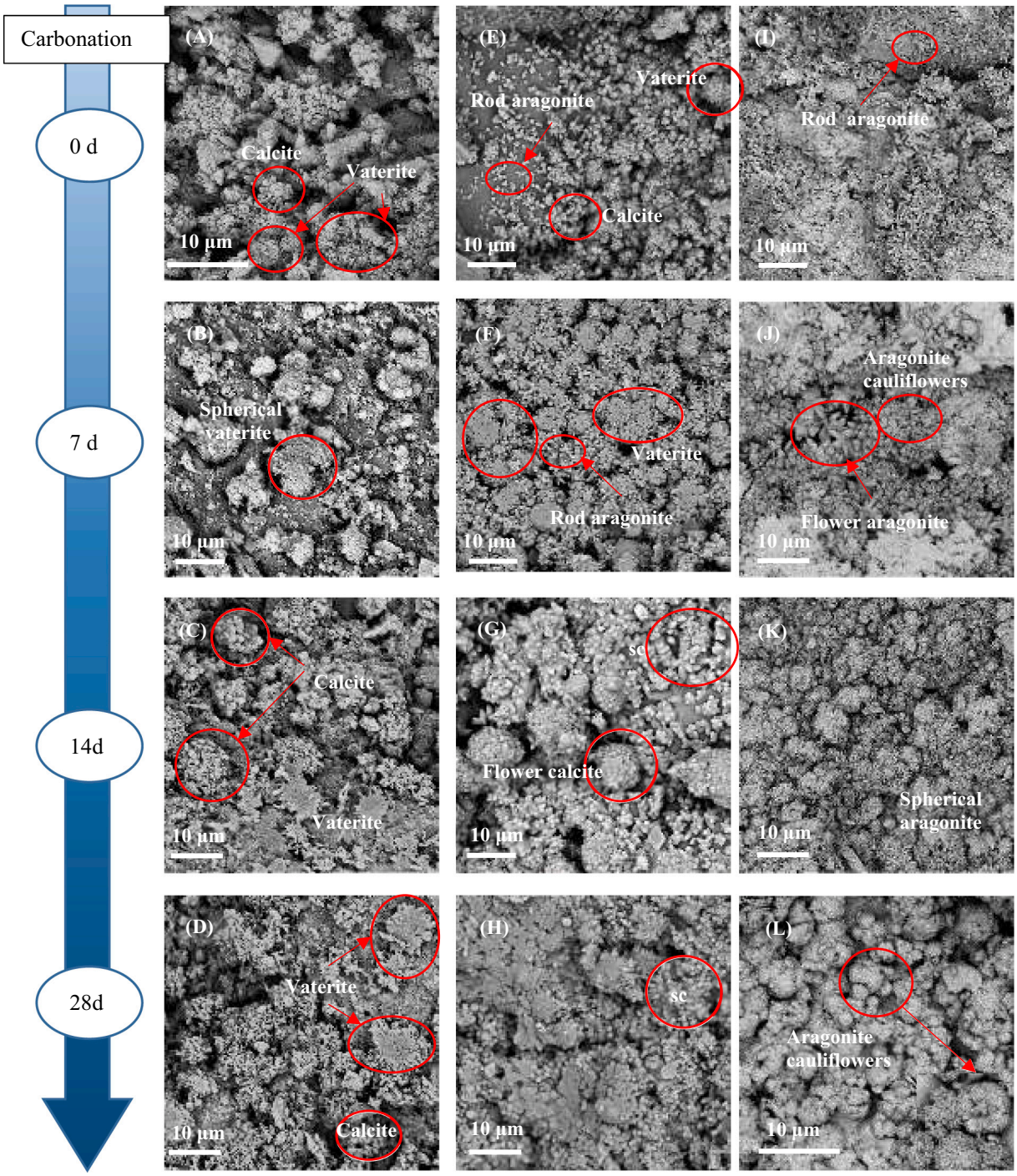

Fig. 12. SEM images of tested mortar samples containing TiO_2 hydrosol before and after accelerating carbonation test (Fig.(A-D) are belong to the reference group; Fig.(*E*-H) are belong to the mortar mixed 0.01 wt% TiO_2; Fig. (I-L) are belong to the mortar mixed 0.50 wt% TiO_2; crystal shape of calcite, sc: scalenorhombohedral).

dosage of TiO_2 hydrosol (>0.05 wt% of cement). Based on the results in Section 3.1 and Section 3.2, the calcium carbonate phase in the sample containing 0.50 wt% TiO_2 has several different polymorphs during carbonation, and the SSA increase induced by carbonation is much smaller than in the other samples. Thus, it is speculated that the recovery of the photocatalytic self-cleaning performance of carbonated mortar is closely related to the physical properties and morphologies of different polymorphs of $CaCO_3$. The relationships between the carbonates and photocatalytic self-cleaning performance will be thoroughly discussed in Section 4.

3.5. Morphology evolution of $CaCO_3$

The SEM images of different mortars at different carbonation time are shown in Fig. 12. Fig. 12(A, E, I) shows that both rhomboscalenohedral calcite crystal and vaterite aggerates are observed on the reference mortar after three days of carbonation. On the surface of mortar with 0.01 wt% TiO_2, rod aragonite crystals are detected besides calcite and vaterite. More rod aragonite crystals are observed on the surface of mortar containing 0.05 wt% TiO_2. In Fig. 12(B, F, J), after seven days of carbonation, the spherical vaterite crystals are observed on the surface of reference mortar, while the vaterite particles tend to merge in the mortar containing 0.01 wt% TiO_2. The rod-shaped aragonite crystals transform into larger flower-shaped and smaller cauliflower-shaped aragonite crystals on the mortar surface containing 0.50 wt% TiO_2. Fig. 12(C, G, K) shows that the spherical vaterite crystals are merged, and the scalenorhombohedral calcite crystals are aggregated on the reference surface. On the surface of mortar with 0.01 wt% TiO_2, aggregates of rhomboscalenohedral calcite crystal, and spherical aggregates of scalenorhombohedral calcite crystals are observed. The flower-shaped aragonite crystals transform into smaller aragonite radiating clusters of tiny prismatic crystals in the mortar with 0.50 wt% TiO_2. In Fig. 12(D, H, L), vaterite and calcite phases are observed on the surface of the reference mortar, and the mortar containing a lower dosage of TiO_2 (<0.05 wt%), while aragonite is the main meta-stable phase of $CaCO_3$ in the surface of mortar sample containing a higher dosage of TiO_2 (>0.05 wt%).

As discussed in Section 3.1.2 and Section 3.2, the TiO_2 hydrosol significantly impacts the crystal sizes and shapes of CH and C-S-H phases in hydrated mortar samples, further affecting the specific surface areas of mortar samples after the curing of 28 days. According to the previous studies [81,82] on the interaction of nitrogen oxides (NO_x) with the nano TiO_2 photocatalytic cement-based materials, the TiO_2 nanoparticles contribute to the NOx absorption increase because of increasing the SSA of the matrix. Moreover, as mentioned in Section 3.1, the mortar containing a higher dosage of TiO_2 shows higher SSA and bigger CH and more fibrillar C-S-H phases. Thus, the addition of nano TiO_2 influences the CO_2 absorption and the crystal solubility in pore solution at the initial period of the carbonation test. As a result, the cement hydrates in the mortar with TiO_2 hydrosol show different morphology evolution during carbonation. In addition, the volume and size of polymorphs of $CaCO_3$ change with the increase of carbonation time, indicating that the coverage effect of $CaCO_3$ on the mortar surface also changes during carbonation.

To further understand the distribution evolution of TiO_2, $CaCO_3$ polymorphs, and main hydrates (Portlandite and C-S-H phase), Fig. 13 (A) shows the Raman images by CRM of mortar samples with 0.50 wt% TiO_2 before and after carbonation. The Raman images of mortar samples containing 0.01 wt%, 0.05 wt% and 0.10 wt% TiO_2 are shown in Fig. S6 in the supplemental file.

According to the previous studies, the Raman band of 144 cm^{-1} [83], 356 cm^{-1} [84], and 667 cm^{-1} [85] are referred as the phase of anatase TiO_2, Portlandite, and C-S-H, respectively. For the polymorphs of $CaCO_3$, the Raman band of 7191 cm^{-1}, 703 cm^{-1}, and 750 cm^{-1} [86–89] refer to the phase of calcite, aragonite, and vaterite, respectively. In Fig. 13, the areas outlined in red, green, violet, blue, light blue, and yellow represent the anatase TiO_2, CH, C-S-H, calcite, aragonite, and vaterite, respectively. The area ratio of each phase in the CRM images is

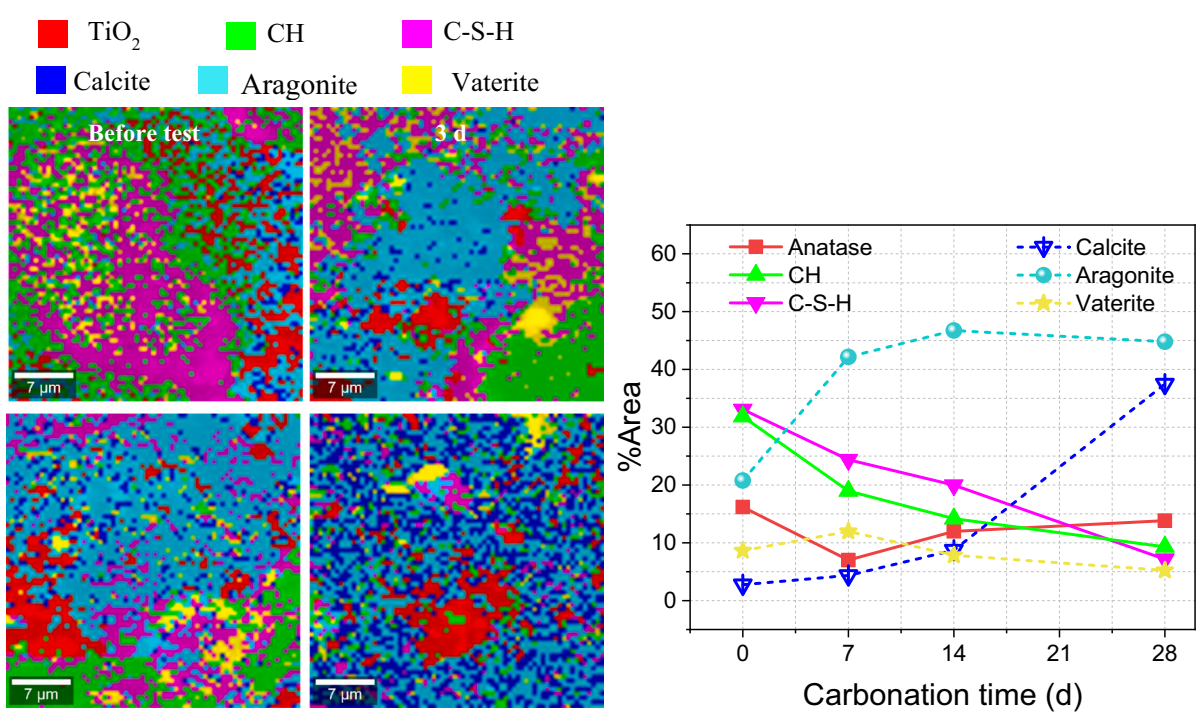

(A) The Raman images (B) Statistical area values vs. carbonation time

Fig. 13. (A) Raman mapping images by CRM of the evolution of the presence of the main phases in the mortar contains 0.50 wt% TiO_2 at different accelerating carbonation test time (the scan area is 35 μm × 35 μm) and (B) Semi-quantitative calculation of the presence of the main phases present of TiO_2 hydrosol modified mortar during the carbonation.

calculated and shown in Fig. 13(B). As shown in Fig. 13, before carbonation, the CH and C-S-H phases are the leading cement hydrates, while the vaterite crystals are scattered around the C-S-H phases, and the aragonite crystals are scattered among the CH, anatase TiO_2, and calcite crystals. After seven days of carbonation, the CH phase is carbonated to aragonite and vaterite. The sphere-shaped vaterite crystals are merged into more massive clusters covering the mortar surface. Simultaneously, the aragonite crystals grow more extensively and cover most areas of the tested surface. After 14 days and 28 days of carbonation, the calcite phase continuously increases due to the further carbonation of CH, aragonite, and vaterite phases, while the anatase TiO_2 crystal increases slightly.

Comparing the results of SEM and CRM of TiO_2 modified mortar, we can conclude that the exposure area of TiO_2 first reduces because of the coverage effect caused by the formed vaterite and aragonite phase at the initial seven days of carbonation. Then the exposure area of the TiO_2 phase regains, mainly because of the crystal shape and pattern evolution of the aragonite phase at a longer carbonation duration. Due to the photochemical reactions on the interfaces between pollution and photocatalysts, the exposure area of the TiO_2 anatase phase on the surface of mortar dominates the self-cleaning performance of TiO_2- mortar catalyst. The essential point is that the chemical reaction between CO_2 and cement hydrates involves a series of crystal phase and shape evolution processes that firmly control the exposure area of TiO_2 in the mortar. These results confirm that the photocatalytic self-cleaning performance of TiO_2 hydrosol modified mortar shows the first declined and then recovered trend, attributed to the crystal morphology evolution of $CaCO_3$ polymorphs caused by carbonation.

4. Discussions

Since the properties of the main hydration products change during the carbonation, the influences of carbonation on the self-cleaning performance need to be considered. The photocatalytic activity of photocatalytic concrete is closely related to the effective exposure surface area of photocatalyst, cement hydrates and carbonates in the matrix surface. Therefore, the discussion of the inter-related roles of individual cement hydrates and carbonates on the photocatalytic self-cleaning performance of mortar is essential to distinguish the significance of each factor.

4.1. Correlation analysis between photocatalytic performance and mortar composition

In this work, the principal factor analysis is used to analyse the influence factors of mortar on the variation of photocatalytic self-cleaning performance during carbonation. Fig. 14 shows the correlation plot among R_{26}, anatase, cement hydrates and carbonates area ratios, carbonation degree (D_c) and carbonation time.

The Spearman correlation coefficient measures the monotonic association between two variables in terms of rank. Spearman correlation coefficients are often used to measure whether one variable increases or decreases with another, even if the relationship between the two variables is not linear or bivariate normal. Considering that the relationships between R_{26} and its influential factors may not be linear, a heat map is used to display the features of the correlation matrix of Spearman correlation coefficients, as shown in Fig. 14. In the correlation matrix, the Spearman's rank correlation coefficient values shown in the lower triangular matrix in Fig. 14 correspond to the colours in the upper triangular matrix.

Spearman's rank correlation coefficients with high absolute values (>0.50) indicate that this variable is monotonous consistent with the output. The asterisks in the upper triangular grids in Fig. 14 mean the *p*-values in the statistical analysis, representing the significant level of

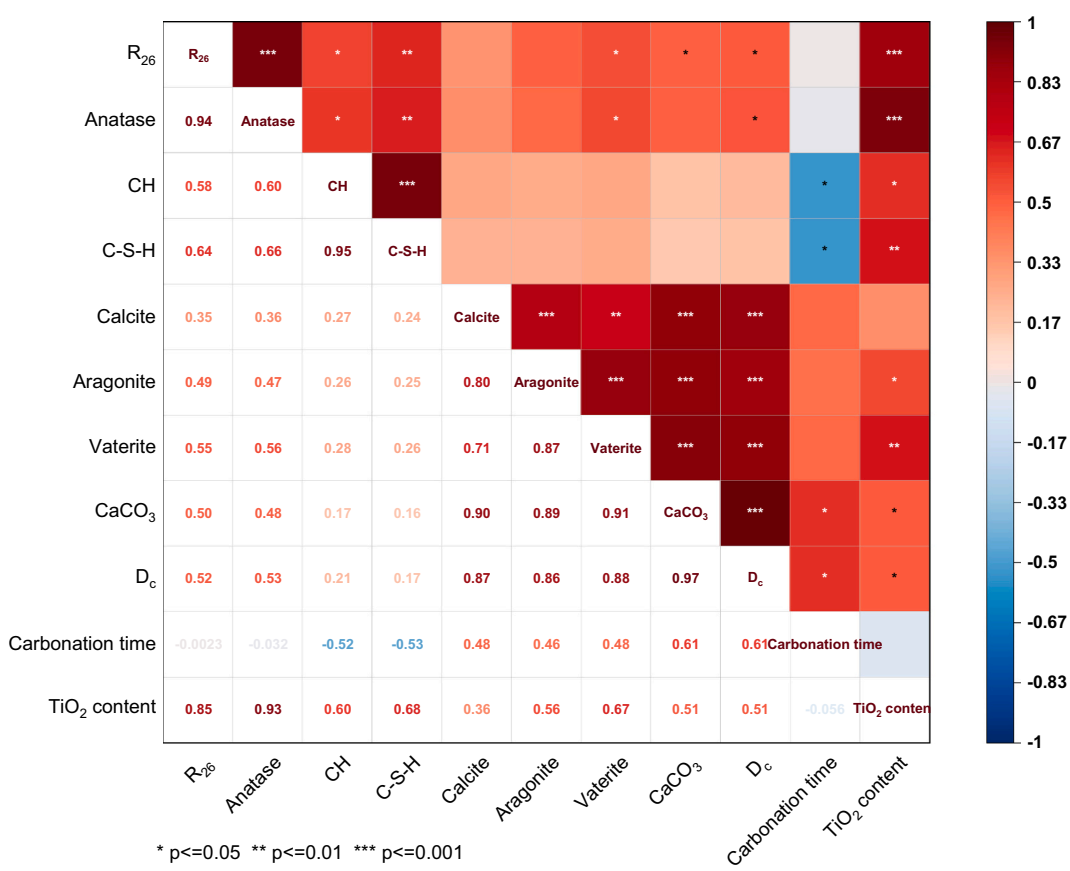

Fig. 14. Correlation matrix of the factors related to the photocatalytic self-cleaning performance.

parameters on the horizontal axis to those on the vertical axis. An asterisk represents the p-value is smaller than 0.05, two asterisks represent the p-value is smaller than 0.01, while three asterisks represent the p-values is smaller than 0.001. For example, the change of R_{26} is monotonously corresponding to the area ratios of anatase, CH, C-S-H, $CaCO_3$ and the TiO_2 content, where the significant levels of the variation of the area ratio of anatase and the TiO_2 content are higher than that of the area ratio of C-S-H.

The anatase area ratio is closely influenced by the variation of CH, C-S-H, D_c and nano TiO_2 content in mortar while changing of D_c is associated with the variation of main cement hydrates and carbonates. As shown in Fig. 14, the total $CaCO_3$ area ratio is mainly monotonously related to the variation of D_c, carbonation time and TiO_2 content. Since both CH and C-S-H area ratios are monotonously related to the variation of the anatase area ratio and the carbonation time that is monotonously corresponding to the variation of D_c, the anatase area ratio and D_c are suitable as characteristic variables of R_{26}. Due to the data being more easily collected, the TiO_2 content is selected as the characteristic variable of anatase area ratio, D_c is selected as the characteristic variable of $CaCO_3$ area ratio in this study. Therefore, it is feasible to establish a prediction model for the changing of R_{26} with the variation of characteristic components of photocatalytic mortar.

4.2. Prediction model of photocatalytic self-cleaning performance during carbonation

Here, the variation of photocatalytic self-cleaning performance of mortar during carbonation can be predicted by two pairs of characteristic variables as mentioned in Section 4.1. A more straightforward intuitional relationship is expected to describe the R_{26} with the variation of anatase and $CaCO_3$ exposure area ratios. The binary functional relationship is established among the R_{26}, anatase area ratio, and $CaCO_3$ area ratio, the simulated 3D surface is shown in Fig. 15, and the following equation can describe the relationship:

$$R_{26} = 32.10 + 2.80\,A_{TiO_2} - 0.46A_{CaCO_3} + 0.03A_{TiO_2}^2 + 0.006A_{CaCO_3}^2 - 0.03A_{TiO_2} \times A_{CaCO_3} \quad (5)$$

The correlation of this fit is 0.95, indicating this binary function can

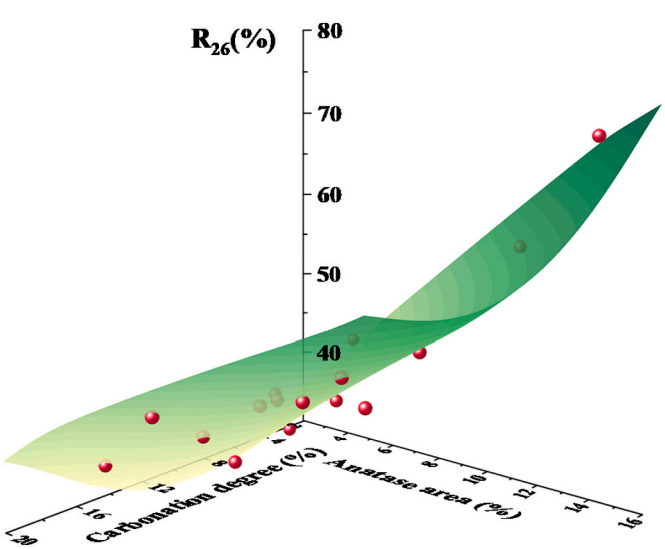

Fig. 15. Simulating surface among R_{26}, anatase and $CaCO_3$ area ratios.

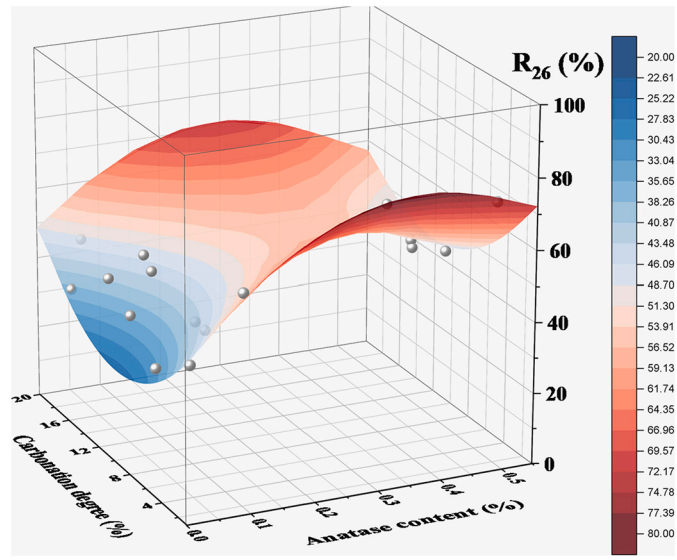

Fig. 16. Simulating surface among R_{26}, anatase content and carbonation degree.

well describe the change law of photocatalytic self-cleaning performance of mortar along with the change of carbonates area.

R_{26} is the percentage of discolouration of RB on the surface of photocatalytic mortar after 26-hour irradiation of UV, representing the photocatalytic self-cleaning ability of mortar; A_{TiO2} and A_{CaCO3} are the area ratios of anatase and calcium carbonates in the surface of photocatalytic mortar detected by CRM, $3.5\% < A_{TiO2} < 12\%$.

Considering the difficulty of obtaining experimental data in the CRM analysis, we propose to quantify the influences of carbonation on the photocatalytic self-cleaning ability of nano TiO_2 hydrosol modified mortar by using the characteristic factors of anatase and $CaCO_3$ area ratios, namely nano TiO_2 (anatase) contents in the mortar and the carbonation degrees of mortar. Fig. 16 and

$$R_{26} = 48.0 + 204.0\,C_{TiO_2} - 4.5D_c - 276C_{TiO_2}^2 + 0.23D_c^2 - 2.17C_{TiO_2} \times D_c \quad (6)$$

present the fitting surface and binary function of the variation of R_{26} along with the variation of nano TiO_2 content and D_c of mortar.

R_{26} is the percentage of discolouration of RB on the surface of photocatalytic mortar after 26-h irradiation of UV; C_{TiO2} is the initial weight content ratio of anatase mixed in the mortar, $0.01\% < C_{TiO2} < 0.5\%$; D_c is the carbonation degree of mortar calculated in Section 3.3.

The proposed model shows an excellent correspondence, with a high fitting degree of 0.93. It should be noted that the functional relationship shown in Eq. (5) is widely applicable because the variable of D_c is more easily collected in the lab than components area ratios. Based on this proposed model, the photocatalytic self-cleaning performances of nano TiO_2 hydrosol modified cementitious materials during carbonation can be calculated if the carbonation degree and the anatase content in mortar are obtained. Nevertheless, the validity of this model for other applications still needs verification. However, the processes of demonstration and the establishment of this model provide a feasible way to clarify the relationship between the hydrates carbonation and the variation of photocatalytic self-cleaning performance of photocatalytic

cement-based materials.

5. Conclusions

This work studies the effects of carbonation on the photo-induced self-cleaning performance of nano TiO_2 hydrosol-modified mortar. The coverage effect of cement hydration products and the evolution of crystal morphology during carbonization are considered in studying the relationship between carbonation and self-cleaning performance of mortar. The following conclusions can be drawn from the acquired results:

(1) Carbonation reduces the self-cleaning performance of the photocatalytic mortar. The photoactivity of TiO_2-mortar is seriously affected by aragonite, vaterite or intermediate products of calcium carbonate. After complete carbonation, a large amount of aragonite and unstable calcium carbonate transforms into stable calcite phase with a smaller volume. The re-exposure of photocatalytic active sites leads to recovery of the self-cleaning performance of the carbonated mortar.
(2) Nano TiO_2 hydrosol affects the carbonation rate of cement hydrates. The amount of nano TiO_2 hydrosol significantly influences the crystal type and volume of carbonation products. When the dosage of nano-TiO_2 is less than or equal to 0.05 wt% of cement, the surface defects of nano-TiO_2 decrease first and then increase with the carbonation time; the carbonation rate of C-S-H dominates the carbonation process of mortar. When the nano-TiO_2 dosage is greater than 0.05 wt% of cement, the surface defects of nano-TiO_2 decrease continuously, and the carbonation rate of CH dominates the carbonation process of mortar.
(3) During carbonation, the self-cleaning ability is closely related to the anatase exposure area ratio and the area ratio of $CaCO_3$ in the mortar surface. The anatase content and the carbonation degree are the characteristic variables of the photocatalytic self-cleaning performance of nano TiO_2 modified mortar during carbonation. A new model is proposed to describe the performance evolution of photocatalytic self-cleaning property of mortar by TiO_2 content and the carbonation degree.

CRediT authorship contribution statement

Zixiao Wang: Methodology, Investigation, Data curation, Formal analysis, Validation, Writing – original draft. **Qingliang Yu:** Conceptualization, Methodology, Supervision, Funding acquisition, Project administration, Writing – review & editing. **Pan Feng:** Resources. **H.J. H. Brouwers:** Writing – review & editing.

Declaration of competing interest

The authors declare that they have no known competing financial interests or personal relationships that could have appeared to influence the work reported in this paper.

Acknowledgments

This work is funded by the National Natural Science Foundation of China (No. 52178246, No. 1706222, No. 51708108), the China Scholarship Council (No. 201806090146), and the Eindhoven University of Technology (TU/e). In addition, the authors gratefully acknowledge M. Sc. Bin Meng (Building Performance group of TU/e) for his help in processing data of self-cleaning performance characterization, Prof. Albert Schenning and M.Sc. Xinglong Pan (Stimuli-responsive Functional Materials & Devices group of TU/e) for their advice and comments on the measurements of the spectral analysis, and M.Sc. Ayberk Özden (Materials and Interface Chemistry group of TU/e) for his comments on the measurements of Confocal Raman Microscopy.

Appendix A. Supplementary data

Supplementary data to this article can be found online at https://doi.org/10.1016/j.cemconres.2022.106852.

References

[1] Q.L. Yu, M.M. Ballari, H.J.H. Brouwers, Indoor air purification using heterogeneous photocatalytic oxidation. Part II: kinetic study, Appl. Catal. B Environ. 99 (2010) 58–65, https://doi.org/10.1016/j.apcatb.2010.05.032.
[2] Q.L. Yu, H.J.H. Brouwers, Indoor air purification using heterogeneous photocatalytic oxidation. Part I: experimental study, Appl. Catal. B Environ. 92 (2009) 454–461, https://doi.org/10.1016/j.apcatb.2009.09.004.
[3] Q.L. Yu, M.M. Ballari, H.J.H. Brouwers, Heterogeneous photocatalysis applied to indoor building material: towards an improved indoor air quality, Adv. Mater. Res. 255–260 (2011) 2836–2840, https://doi.org/10.4028/www.scientific.net/AMR.255-260.2836.
[4] Q.L. Yu, Y. Hendrix, S. Lorencik, H.J.H. Brouwers, Field study of NO_x degradation by a mineral-based air purifying paint, Build. Environ. 142 (2018) 70–82, https://doi.org/10.1016/j.buildenv.2018.06.014.
[5] M.V. Diamanti, M. Ormellese, M. Pedeferri, Characterization of photocatalytic and superhydrophilic properties of mortars containing titanium dioxide, Cem. Concr. Res. 38 (2008) 1349–1353, https://doi.org/10.1016/j.cemconres.2008.07.003.
[6] M.V. Diamanti, B. Del Curto, M. Ormellese, M.P. Pedeferri, Photocatalytic and self-cleaning activity of colored mortars containing TiO_2, Constr. Build. Mater. 46 (2013) 167–174, https://doi.org/10.1016/j.conbuildmat.2013.04.038.
[7] F. Gherardi, A. Colombo, M. D'Arienzo, B. Di Credico, S. Goidanich, F. Morazzoni, R. Simonutti, L. Toniolo, Efficient self-cleaning treatments for built heritage based on highly photo-active and well-dispersible TiO_2 nanocrystals, Microchem. J. 126 (2016) 54–62, https://doi.org/10.1016/j.microc.2015.11.043.
[8] Q. Jin, M. Faraldos, A. Bahamonde, B.H. Zaribaf, K.E. Kurtis, Titania and silica nanoparticle-modified coatings for cementitious materials, in: ACI Symp. Publ, 2019, pp. 97–111.
[9] Z. Wang, P. Feng, H. Chen, Q. Yu, Photocatalytic performance and dispersion stability of nanodispersed TiO_2 hydrosol in electrolyte solutions with different cations, J. Environ. Sci. 88 (2020) 59–71, https://doi.org/10.1016/j.jes.2019.07.013.
[10] E. Burunkaya, M. Akarsu, H. Erdem Çamurlu, Ö. Kesmez, Z. Yeşil, M. Asiltürk, E. Arpaç, Production of stable hydrosols of crystalline TiO_2 nanoparticles synthesized at relatively low temperatures in diverse media, Appl. Surf. Sci. 265 (2013) 317–323, https://doi.org/10.1016/j.apsusc.2012.11.003.
[11] T. Liu, F. Li, X. Li, TiO_2 hydrosols with high activity for photocatalytic degradation of formaldehyde in a gaseous phase, J. Hazard. Mater. 152 (2008) 347–355, https://doi.org/10.1016/j.jhazmat.2007.07.003.
[12] T.X. Liu, Y. Liu, Z.J. Zhang, F.B. Li, X.Z. Li, Comparison of aqueous photoreactions with TiO_2 in its hydrosol solution and powdery suspension for light utilization, Ind. Eng. Chem. Res. 50 (2011) 7841–7848, https://doi.org/10.1021/ie102584j.
[13] N. Serpone, D. Lawless, R. Khairutdinov, Size effects on the photophysical properties of colloidal anatase TiO_2 particles: size quantization versus direct transitions in this indirect semiconductor? J. Phys. Chem. 99 (2002) 16646–16654, https://doi.org/10.1021/j100045a026.
[14] M. Lackhoff, X. Prieto, N. Nestle, F. Dehn, R. Niessner, Photocatalytic activity of semiconductor-modified cement—influence of semiconductor type and cement ageing, Appl. Catal. B Environ. 43 (2003) 205–216, https://doi.org/10.1016/S0926-3373(02)00303-X.
[15] L. Cardellicchio, Self-cleaning and colour-preserving efficiency of photocatalytic concrete: case study of the Jubilee Church in Rome, Build. Res. Inf. (2019) 1–20, https://doi.org/10.1080/09613218.2019.1622405.
[16] E. Jimenez-Relinque, I. Llorente, M. Castellote, TiO_2 cement-based materials: understanding optical properties and electronic band structure of complex matrices, Catal. Today 287 (2017) 203–209, https://doi.org/10.1016/j.cattod.2016.11.015.
[17] A. Hartmann, D. Schulenberg, J. Buhl, Synthesis and structural characterization of CSH-phases in the range of C/S = 0.41 - 1.66 at temperatures of the tobermorite xonotlite crossover, J. Mater. Sci Chem. Eng. 03 (2015) 39–55, https://doi.org/10.4236/msce.2015.311006.
[18] M. Castellote, L. Fernandez, C. Andrade, C. Alonso, Chemical changes and phase analysis of OPC pastes carbonated at different CO_2 concentrations, Mater. Struct. Constr. 42 (2009) 515–525, https://doi.org/10.1617/s11527-008-9399-1.
[19] G.W. Groves, D.I. Rodway, I.G. Richardson, The carbonation of hardened cement pastes, Adv. Cem. Res. 3 (1990) 117–125, https://doi.org/10.1680/adcr.1990.3.11.117.
[20] D.J. Anstice, C.L. Page, M.M. Page, The pore solution phase of carbonated cement pastes, Cem. Concr. Res. 35 (2005) 377–383, https://doi.org/10.1016/j.cemconres.2004.06.041.
[21] M. Auroy, S. Poyet, P. Le Bescop, J.M. Torrenti, T. Charpentier, M. Moskura, X. Bourbon, Comparison between natural and accelerated carbonation (3% CO_2): impact on mineralogy, microstructure, water retention and cracking, Cem. Concr. Res. 109 (2018) 64–80, https://doi.org/10.1016/j.cemconres.2018.04.012.
[22] C. Xiantuo, Z. Ruizhen, C. Xiaorong, Kinetic study of ettringite carbonation reaction, Cem. Concr. Res. 24 (1994) 1383–1389, https://doi.org/10.1016/0008-8846(94)90123-6.

[23] T. Nishikawa, K. Suzuki, S. Ito, K. Sato, T. Takebe, Decomposition of synthesized ettringite by carbonation, Cem. Concr. Compos. 22 (1992) 6–12, https://doi.org/10.20595/jjbf.19.0_3.

[24] Q. Zhou, F.P. Glasser, Kinetics and mechanism of the carbonation of ettringite, Adv. Cem. Res. 12 (2000) 131–136, https://doi.org/10.1680/adcr.2000.12.3.131.

[25] L. Black, C. Breen, J. Yarwood, K. Garbev, P. Stemmermann, B. Gasharova, Structural features of C-S-H(I) and its carbonation in air— a raman spectroscopic study. Part II: carbonated phases, J. Am. Ceram. Soc. 90 (2007) 908–917, https://doi.org/10.1111/j.1551-2916.2006.01429.x.

[26] A. Morandeau, M. Thiéry, P. Dangla, Investigation of the carbonation mechanism of CH and C-S-H in terms of kinetics, microstructure changes and moisture properties, Cem. Concr. Res. 56 (2014) 153–170, https://doi.org/10.1016/j.cemconres.2013.11.015.

[27] M.V. Diamanti, F. Lollini, M.P. Pedeferri, L. Bertolini, Mutual interactions between carbonation and titanium dioxide photoactivity in concrete, Build. Environ. 62 (2013) 174–181, https://doi.org/10.1016/j.buildenv.2013.01.023.

[28] A.M. Kaja, H.J.H. Brouwers, Q.L. Yu, NO_x degradation by photocatalytic mortars: the underlying role of the CH and C-S-H carbonation, Cem. Concr. Res. 125 (2019), https://doi.org/10.1016/j.cemconres.2019.105805.

[29] E. Drouet, S. Poyet, P. Le Bescop, J.M. Torrenti, X. Bourbon, Carbonation of hardened cement pastes: influence of temperature, Cem. Concr. Res. 115 (2019) 445–459, https://doi.org/10.1016/j.cemconres.2018.09.019.

[30] S. von Greve-Dierfeld, B. Lothenbach, A. Vollpracht, B. Wu, B. Huet, C. Andrade, C. Medina, C. Thiel, E. Gruyaert, H. Vanoutrive, I.F.Saéz del Bosque, I. Ignjatovic, J. Elsen, J.L. Provis, K. Scrivener, K.C. Thienel, K. Sideris, M. Zajac, N. Alderete, Ö. Cizer, P.Van den Heede, R.D. Hooton, S. Kamali-Bernard, S.A. Bernal, Z. Zhao, Z. Shi, N.De Belie, Understanding the Carbonation of Concrete With Supplementary Cementitious Materials: A Critical Review by RILEM TC 281-CCC, 2020, https://doi.org/10.1617/s11527-020-01558-w.

[31] A. Leemann, F. Moro, Carbonation of concrete: the role of CO_2 concentration, relative humidity and CO_2 buffer capacity, Mater. Struct. 50 (2017) 1–14, https://doi.org/10.1617/s11527-016-0917-2.

[32] Y. Li, W. Liu, F. Xing, S. Wang, L. Tang, S. Lin, Z. Dong, Carbonation of the synthetic calcium silicate hydrate (C-S-H) under different concentrations of CO_2: chemical phases analysis and kinetics, J. CO2 Util. 35 (2020) 303–313, https://doi.org/10.1016/j.jcou.2019.10.001.

[33] J. Chang, Y. Fang, Quantitative analysis of accelerated carbonation products of the synthetic calcium silicate hydrate (C-S-H) by QXRD and TG/MS, J. Therm. Anal. Calorim. 119 (2015) 57–62, https://doi.org/10.1007/s10973-014-4093-8.

[34] M. Fernández Bertos, S.J.R. Simons, C.D. Hills, P.J. Carey, A review of accelerated carbonation technology in the treatment of cement-based materials and sequestration of CO_2, J. Hazard. Mater. 112 (2004) 193–205, https://doi.org/10.1016/j.jhazmat.2004.04.019.

[35] J.M. Marangu, J.K. Thiong'O, J.M. Wachira, Review of carbonation resistance in hydrated cement based materials, J. Chem. 2019 (2019), https://doi.org/10.1155/2019/8489671.

[36] I. Galan, C. Andrade, M. Castellote, Natural and accelerated CO_2 binding kinetics in cement paste at different relative humidities, Cem. Concr. Res. 49 (2013) 21–28, https://doi.org/10.1016/j.cemconres.2013.03.009.

[37] F. Georget, W. Soja, K.L. Scrivener, Characteristic lengths of the carbonation front in naturally carbonated cement pastes: implications for reactive transport models, Cem. Concr. Res. 134 (2020), 106080, https://doi.org/10.1016/j.cemconres.2020.106080.

[38] I. Monteiro, F.A. Branco, J. De Brito, R. Neves, Statistical analysis of the carbonation coefficient in open air concrete structures, Constr. Build. Mater. 29 (2012) 263–269, https://doi.org/10.1016/j.conbuildmat.2011.10.028.

[39] R. Neves, F. Branco, J. De Brito, Field assessment of the relationship between natural and accelerated concrete carbonation resistance, Cem. Concr. Compos. 41 (2013) 9–15, https://doi.org/10.1016/j.cemconcomp.2013.04.006.

[40] X. Gan, K. He, B. Qian, Q. Deng, L. Lu, Y. Wang, The effect of glycine on the growth of calcium carbonate in alkaline silica gel, J. Cryst. Growth 458 (2017) 60–65, https://doi.org/10.1016/j.jcrysgro.2016.11.027.

[41] R. Ševčík, M. Pérez-Estébanez, A. Viani, P. Šašek, P. Mácová, Characterization of vaterite synthesized at various temperatures and stirring velocities without use of additives, Powder Technol. 284 (2015) 265–271, https://doi.org/10.1016/j.powtec.2015.06.064.

[42] F.C. Meldrum, Calcium carbonate in biomineralisation and biomimetic chemistry, Int. Mater. Rev. 48 (2003) 187–224, https://doi.org/10.1179/095066003225005836.

[43] Y. Ding, Y. Liu, Y. Ren, H. Yan, M. Wang, D. Wang, X.Y. Lu, B. Wang, T. Fan, H. Guo, Controllable synthesis of all the anhydrous $CaCO_3$ polymorphs with various morphologies in $CaCl_2$-NH_3-CO_2 aqueous system, Powder Technol. 333 (2018) 410–420, https://doi.org/10.1016/j.powtec.2018.04.056.

[44] E.T. Stepkowska, M.A. Aviles, J.M. Blanes, J.L. Perez-Rodriguez, Gradual transformation of $Ca(OH)_2$ into $CaCO_3$ on cement hydration XRD study, J. Therm. Anal. Calorim. 87 (2007) 189–198, https://doi.org/10.1007/s10973-006-7840-7.

[45] Z. Wang, Q. Yu, F. Gauvin, P. Feng, R. Qianping, H.J.H. Brouwers, Nanodispersed TiO_2 hydrosol modified Portland cement paste: the underlying role of hydration on self-cleaning mechanisms, Cem. Concr. Res. 136 (2020), https://doi.org/10.1016/j.cemconres.2020.106156.

[46] M.V. Diamanti, R. Paolini, M. Rossini, A.B. Aslan, M. Zinzi, T. Poli, M.P. Pedeferri, Long term self-cleaning and photocatalytic performance of anatase added mortars exposed to the urban environment, Constr. Build. Mater. 96 (2015) 270–278, https://doi.org/10.1016/j.conbuildmat.2015.08.028.

[47] V.S. Harutyunyan, A.P. Kirchheim, P.J.M. Monteiro, A.P. Aivazyan, P. Fischer, Investigation of early growth of calcium hydroxide crystals in cement solution by soft X-ray transmission microscopy, J. Mater. Sci. 44 (2009) 962–969, https://doi.org/10.1007/s10853-008-3198-5.

[48] R. López, R. Gómez, Band-gap energy estimation from diffuse reflectance measurements on sol-gel and commercial TiO_2: a comparative study, J. Sol-Gel Sci. Technol. 61 (2012) 1–7, https://doi.org/10.1007/s10971-011-2582-9.

[49] D.C. Cronemeyer, Electrical and optical properties of rutile single crystals, Phys. Rev. 87 (1952) 876–886, https://doi.org/10.1103/PhysRev.87.876.

[50] Franz Urbach, The long-wavelength edge of photographic sensitivity and of the electronic absorption of solids, Phys. Rev. 92 (1953), https://doi.org/10.1103/PhysRev.92.1324, 1324–1324.

[51] S. Tsivilis, G. Kakali, E. Chaniotakis, A. Souvaridou, A study on the hydration of Portland limestone cement by means of TG, J. Therm. Anal. Calorim. 52 (1998) 863–870, https://doi.org/10.1023/A:1010139312958.

[52] G. Kakali, S. Tsivilis, A. Tsialtas, Hydration of ordinary Portland cements made from raw mix containing transition element oxides, Cem. Concr. Res. 28 (1998) 335–340, https://doi.org/10.1016/S0008-8846(97)00250-0.

[53] I. Pane, W. Hansen, Investigation of blended cement hydration by isothermal calorimetry and thermal analysis, Cem. Concr. Res. 35 (2005) 1155–1164, https://doi.org/10.1016/j.cemconres.2004.10.027.

[54] G. Villain, M. Thiery, G. Platret, Measurement methods of carbonation profiles in concrete: thermogravimetry, chemical analysis and gammadensimetry, Cem. Concr. Res. 37 (2007) 1182–1192, https://doi.org/10.1016/j.cemconres.2007.04.015.

[55] X. Pan, C. Shi, X. Hu, Z. Ou, Effects of CO_2 surface treatment on strength and permeability of one-day-aged cement mortar, Constr. Build. Mater. 154 (2017) 1087–1095, https://doi.org/10.1016/j.conbuildmat.2017.07.216.

[56] Z. Tu, M.Z. Guo, C.S. Poon, C. Shi, Effects of limestone powder on $CaCO_3$ precipitation in CO_2 cured cement pastes, Cem. Concr. Compos. 72 (2016) 9–16, https://doi.org/10.1016/j.cemconcomp.2016.05.019.

[57] F. Matsushita, Y. Aono, S. Shibata, Carbonation degree of autoclaved aerated concrete, Cem. Concr. Res. 30 (2000) 1741–1745, https://doi.org/10.1016/S0008-8846(00)00424-5.

[58] E. Cerro-Prada, M. Manso, V. Torres, J. Soriano, Microstructural and photocatalytic characterization of cement-paste sol-gel synthesized titanium dioxide, front. StructCiv. Eng. 10 (2016) 189–197, https://doi.org/10.1007/s11709-015-0326-6.

[59] D. Feng, N. Xie, C. Gong, Z. Leng, H. Xiao, H. Li, X. Shi, Portland cement paste modified by TiO_2 nanoparticles: a microstructure perspective, Ind. Eng. Chem. Res. 52 (2013) 11575–11582, https://doi.org/10.1021/ie4011595.

[60] S. Steiner, B. Lothenbach, T. Proske, A. Borgschulte, F. Winnefeld, Effect of relative humidity on the carbonation rate of portlandite, calcium silicate hydrates and ettringite, Cem. Concr. Res. 135 (2020), 106116, https://doi.org/10.1016/j.cemconres.2020.106116.

[61] L. Black, K. Garbev, I. Gee, Surface carbonation of synthetic C-S-H samples: a comparison between fresh and aged C-S-H using X-ray photoelectron spectroscopy, Cem. Concr. Res. 38 (2008) 745–750, https://doi.org/10.1016/j.cemconres.2008.02.003.

[62] M.G. Margalha, A.S. Silva, M.D.R. Veiga, J. De Brito, R.J. Ball, G.C. Allen, Microstructural changes of lime putty during aging, J. Mater. Civ. Eng. 25 (2013) 1524–1532, https://doi.org/10.1061/(ASCE)MT.1943-5533.0000687.

[63] E. Ruiz-Agudo, K. Kudłacz, C.V. Putnis, A. Putnis, C. Rodriguez-Navarro, Dissolution and carbonation of portlandite [$Ca(OH)_2$] single crystals, Environ. Sci. Technol. 47 (2013) 11342–11349, https://doi.org/10.1021/es402061c.

[64] G. Mascolo, M.C. Mascolo, A. Vitale, O. Marino, Microstructure evolution of lime putty upon aging, J. Cryst. Growth 312 (2010) 2363–2368, https://doi.org/10.1016/j.jcrysgro.2010.05.020.

[65] R. Camerini, G. Poggi, D. Chelazzi, F. Ridi, R. Giorgi, P. Baglioni, The carbonation kinetics of calcium hydroxide nanoparticles: a boundary nucleation and growth description, J. Colloid Interface Sci. 547 (2019) 370–381, https://doi.org/10.1016/j.jcis.2019.03.089.

[66] C. Rodriguez-Navarro, K. Elert, R. Ševčík, Amorphous and crystalline calcium carbonate phases during carbonation of nanolimes: implications in heritage conservation, CrystEngComm 18 (2016) 6594–6607, https://doi.org/10.1039/c6ce01202g.

[67] L.S. Gomez-Villalba, P. López-Arce, M. Alvarez De Buergo, R. Fort, Atomic defects and their relationship to aragonite-calcite transformation in portlandite nanocrystal carbonation, Cryst. Growth Des. 12 (2012) 4844–4852, https://doi.org/10.1021/cg300628m.

[68] P. López-Arce, L.S. Gómez-Villalba, S. Martínez-Ramírez, M. Álvarez de Buergo, R. Fort, Influence of relative humidity on the carbonation of calcium hydroxide nanoparticles and the formation of calcium carbonate polymorphs, Powder Technol. 205 (2011) 263–269, https://doi.org/10.1016/j.powtec.2010.09.026.

[69] Ö. Cizer, C. Rodriguez-Navarro, E. Ruiz-Agudo, J. Elsen, D. Van Gemert, K. Van Balen, Phase and morphology evolution of calcium carbonate precipitated by carbonation of hydrated lime, J. Mater. Sci. 47 (2012) 6151–6165, https://doi.org/10.1007/s10853-012-6535-7.

[70] O. Cazalla, C. Rodriguez-Navarro, E. Sebastian, G. Cultrone, M.J. De la Torre, Aging of lime putty: effects on traditional lime mortar carbonation, J. Am. Ceram. Soc. 83 (2000) 1070–1076, https://doi.org/10.1111/j.1151-2916.2000.tb01332.x.

[71] K. Elert, C. Rodriguez-Navarro, E.S. Pardo, E. Hansen, O. Cazalla, Lime mortars for the conservation of historic buildings, Stud. Conserv. 47 (2002) 62–75, https://doi.org/10.1179/sic.2002.47.1.62.

[72] A. Trapote-Barreira, J. Cama, J.M. Soler, Dissolution kinetics of C-S-H gel: Flow-through experiments, Phys. Chem. Earth 70–71 (2014) 17–31, https://doi.org/10.1016/j.pce.2013.11.003.

[73] R. Amadelli, L. Samiolo, M. Borsa, M. Bellardita, L. Palmisano, N-TiO_2 photocatalysts highly active under visible irradiation for NO_x abatement and 2-

propanol oxidation, Catal. Today 206 (2013) 19–25, https://doi.org/10.1016/j.cattod.2011.11.031.

[74] M. Gao, L. Zhu, W.L. Ong, J. Wang, G.W. Ho, Structural design of TiO_2 -based photocatalyst for H_2 production and degradation applications, Catal.Sci. Technol. 5 (2015) 4703–4726, https://doi.org/10.1039/c5cy00879d.

[75] R. Bhatt, I. Bhaumik, S. Ganesamoorthy, A.K. Karnal, M.K. Swami, H.S. Patel, P. K. Gupta, Urbach tail and bandgap analysis in near stoichiometric $LiNbO_3$ crystals, Phys. Status Solidi Appl. Mater. Sci. 209 (2012) 176–180, https://doi.org/10.1002/pssa.201127361.

[76] M.M. Khan, S.A. Ansari, D. Pradhan, M.O. Ansari, D.H. Han, J. Lee, M.H. Cho, Band gap engineered TiO_2 nanoparticles for visible light induced photoelectrochemical and photocatalytic studies, J. Mater. Chem. A 2 (2014) 637–644, https://doi.org/10.1039/c3ta14052k.

[77] V. Nadtochenko, N. Denisov, A. Gorenberg, Y. Kozlov, P. Chubukov, J.A. Rengifo, C. Pulgarin, J. Kiwi, Correlations for photocatalytic activity and spectral features of the absorption band edge of TiO_2 modified by thiourea, Appl. Catal. B Environ. 91 (2009) 460–469, https://doi.org/10.1016/j.apcatb.2009.06.015.

[78] B. Choudhury, A. Choudhury, Oxygen defect dependent variation of band gap, urbach energy and luminescence property of anatase, anatase-rutile mixed phase and of rutile phases of TiO_2 nanoparticles, Phys. E: Low-Dimens. Syst. Nanostructures 56 (2014) 364–371, https://doi.org/10.1016/j.physe.2013.10.014.

[79] E. Jimenez-Relinque, J.R. Rodriguez-Garcia, A. Castillo, M. Castellote, Characteristics and efficiency of photocatalytic cementitious materials: type of binder, roughness and microstructure, Cem. Concr. Res. 71 (2015) 124–131, https://doi.org/10.1016/j.cemconres.2015.02.003.

[80] S. Karapati, T. Giannakopoulou, N. Todorova, N. Boukos, S. Antiohos, D. Papageorgiou, E. Chaniotakis, D. Dimotikali, C. Trapalis, TiO_2 functionalization for efficient NO_x removal in photoactive cement, Appl. Surf. Sci. 319 (2014) 29–36, https://doi.org/10.1016/j.apsusc.2014.07.162.

[81] Q. Jin, E.M. Saad, W. Zhang, Y. Tang, K.E. Kurtis, Quantification of NO_x uptake in plain and TiO_2 -doped cementitious materials, Cem. Concr. Res. 122 (2019) 251–256, https://doi.org/10.1016/j.cemconres.2019.05.010.

[82] Q. Jin, S.L. Hordern, Y. Tang, K.E. Kurtis, NO_x sequestration by calcium aluminate cementitious materials, Cem. Concr. Res. 142 (2021), 106381, https://doi.org/10.1016/j.cemconres.2021.106381.

[83] M. Torres-Carrasco, A. del Campo, M.A. de la Rubia, E. Reyes, A. Moragues, J. F. Fernández, New insights in weathering analysis of anhydrous cements by using high spectral and spatial resolution confocal raman microscopy, Cem. Concr. Res. 100 (2017) 119–128, https://doi.org/10.1016/j.cemconres.2017.06.003.

[84] T. Schmida, P. Dariz, Shedding light onto the spectra of lime: raman and luminescence bands of CaO, $Ca(OH)_2$ and $CaCO_3$, J. Raman Spectrosc. 46 (2015) 141–146, https://doi.org/10.1002/jrs.4622.

[85] J. Higl, M. Köhler, M. Lindén, Confocal raman microscopy as a non-destructive tool to study microstructure of hydrating cementitious materials, Cem. Concr. Res. 88 (2016) 136–143, https://doi.org/10.1016/j.cemconres.2016.07.005.

[86] G. Gao, P. Huang, K. Wang, R. He, D. Cui, Gram-scale synthesis and shape evolution of micro-$CaCO_3$, Powder Technol. 205 (2011) 270–275, https://doi.org/10.1016/j.powtec.2010.09.032.

[87] U. Wehrmeister, A.L. Soldati, D.E. Jacob, T. Häger, W. Hofmeister, Raman spectroscopy of synthetic, geological and biological vaterite: a raman spectroscopic study, J. Raman Spectrosc. 41 (2010) 193–201, https://doi.org/10.1002/jrs.2438.

[88] J.D. Rodriguez-Blanco, S. Shaw, L.G. Benning, The kinetics and mechanisms of amorphous calcium carbonate (ACC) crystallization to calcite, via vaterite, Nanoscale 3 (2011) 265–271, https://doi.org/10.1039/c0nr00589d.

[89] Z. Zhang, Y. Xie, X. Xu, H. Pan, R. Tang, Transformation of amorphous calcium carbonate into aragonite, J. Cryst. Growth 343 (2012) 62–67, https://doi.org/10.1016/j.jcrysgro.2012.01.025.